Reverberation Mapping Analysis of the 2016 HST Campaign on NGC 4593

Lukas Diehl

George-August-Universität Göttingen

February 21, 2026

Abstract

Abstract

Contents

List of Figures

List of Tables

1. Introduction

Active galactic nuclei (AGNs) are among the most luminous objects in the universe, emitting radiation across the entire electromagnetic spectrum (Netzer 2013) and exhibiting strong variability on timescales ranging from hours to days (Ulrich et al. 1997). In contrast to inactive galaxies such as the Milky Way, the supermassive black hole (SMBH) in an active galaxy accretes matter from the central region. This process generates thermal emission from the accretion flow (Peterson 1997) and drives line emission through photoionization and subsequent recombination in the surrounding gas (Netzer 2013). These ionized line-emitting regions are commonly divided into the broad-line region (BLR) and the narrow-line region (NLR) (Peterson 1997). The BLR is located at close distances of light-days to a few light-years from the central SMBH (Goad et al. 2012) and rotates at high velocities of several thousand $km\,s^{-1}$, which leads to strong Doppler broadening of the emission lines (Peterson 1997). In contrast, the NLR extends out to several hundred parsecs from the central region (Peterson 1997) with velocities of only a few hundred $km\,s^{-1}$, resulting in comparatively narrow line profiles.

An interesting example of this class of objects is the barred spiral galaxy NGC 4593. It shows pronounced variability from the X-ray to the optical bands (McHardy et al. 2017; Cackett et al. 2018) and exhibits several prominent broad emission lines, including Balmer and helium lines, as well as low-ionization lines like O I $\lambda8446$ (Kollatschny & Dietrich 1997; Cackett et al. 2018; Ochmann et al. 2025). Several studies on NGC 4593 have analyzed the structure and kinematics of its broad-line region (e.g. Kollatschny & Dietrich 1997; Denney et al. 2006; Cackett et al. 2018) using reverberation mapping (RM) of the broad emission lines. This method uses measurable time delays between variations in the ionizing continuum and the response of the line-emitting gas to infer the characteristic size and geometry of the broad-line region (Peterson 1993).

In a recent study, Cackett et al. 2018 carried out an observation campaign using the Hubble Space Telescope (HST) with the Space Telescope Imaging Spectrograph (STIS), between 12 July and 6 August 2016, on NGC 4593 covering wavelength

ranges of approximately $1100\,\text{Å} - 1700\,\text{Å}$ and $3900\,\text{Å} - 9000\,\text{Å}$. This campaign focused on the reverberation of the accretion disk of NGC 4593 by analyzing the UV and optical continua (Cackett et al. 2018). However, a RM analysis of the BLR has not been attempted with this dataset. As a HST dataset, it is ideally suited for a RM analysis, thanks to its daily cadence and broad wavelength coverage. It allows a more detailed structural analysis of the BLR of NGC 4593 compared to earlier campaigns (Kollatschny & Dietrich 1997; Denney et al. 2006; Williams et al. 2018) by including broad emission lines to the analysis, which have not been monitored for NGC 4593 yet (e.g. UV emission lines).

Furthermore, NGC 4593 shows variability in the low-ionization O I $\lambda8446$ line and the Ca II $\lambda8498\,\lambda8542\,\lambda8662$ triplet (Ochmann et al. 2025), which have not been included in RM campaigns so far. The O I $\lambda8446$ line is particularly interesting because its strength can be enhanced by Bowen fluorescence (Bowen 1947; Grandi 1980). Since it is covered by the Cackett et al. 2018 campaign, its variability and time lag to can be measured and its Bowen fluorescence process investigated in a RM analysis for the first time.

2. Scientific Background

2.1 Active Galactic Nuclei

Active Galactic Nuclei (AGNs) refer to the central region of active galaxies. These objects are among the most luminous in the universe, with bolometric luminosities ranging from 10^{41} to 10^{48} erg s^{-1} that can outshining entire galaxies by several orders of magnitude (Peterson 1997). Historically, several stellar-based models were proposed for AGNs, such as dense star clusters or supermassive stars. However, these scenarios were discarded, as they are expected to collapse into black holes themselves, and they cannot provide the required energy output. Today, it is understood that the enormous luminosities of AGN are powered by accretion of matter onto a supermassive black hole (SMBH) at the centers of galaxies (Rees 1984). The most widely accepted model for this accretion is a hot, rotating accretion disk surrounding the SMBH, which produces most of the observed radiation (Shakura & Sunyaev 1973). The following sections will outline the key components of AGNs and their variability, which is central to reverberation mapping analysis.

Figure 2.1: Different components of an AGN. Adopted from (Mo et al. 2010). Their Figure 14.3.

2.1.1 Geometric and Spectral Features of AGNs

According to the unified model, AGNs consists of a central supermassive black hole (SMBH), a surrounding accretion disk, a dusty torus and ionized gas regions known as the broad-line region (BLR) and narrow-line region (NLR) (Antonucci 1993). In some cases, relativistic jets are launched perpendicular to the plane of the accretion disc (Urry & Padovani 1995). A schematic illustration is shown in Figure 2.1. The following sections describe the physical components of AGN and the spectral features associated with them.

Supermassive Black Hole and Accretion Disk

The center of an AGN is defined by a supermassive black hole (SMBH), with typical masses between $10^6 \, M_\odot$ and $10^9 \, M_\odot$ (Peterson et al. 2004). It does not contribute to the AGN spectrum directly, but acts as the central engine driving observed spectral features of the AGN. It dominates the gravitational potential and, unlike inactive galaxies such as the Milky Way, it is surrounded by an accretion disk. Through viscous processes within the disk, such as turbulent friction and magneto-rotational instability, the angular momentum of the matter is transported outward, which leads to a spiraling inflow of matter toward the SMBH (Shakura & Sunyaev 1973). Several models have been proposed to describe the accretion process. The most widely used model is the geometrically thin and optically thick accretion disk, which consists of ionized gas in differential rotation around the SMBH (Shakura & Sunyaev 1973; Netzer 2013). The disk is composed primarily of ionized hydrogen and helium, with trace amounts of heavier elements (Netzer 2013). The radial extent of the disk is relatively small compared to galactic scales and typically ranges from a few light-hours to a few light-days, corresponding to about 10^{-3} to 10^{-2} pc (Shakura & Sunyaev 1973; Netzer 2013).

During the accretion process a substantial fraction of the gravitational energy of the matter is transformed into thermal radiation, which accounts for the enormous luminosity observed in AGNs and heats the accretion disk to high temperatures that depend on the mass of the SMBH (Netzer 2013). For example, the maximum effective temperature for an accretion disk around a SMBH with $M = 10^8, M_\odot$ is on the order of several $\times 10^5$ K, leading to UV and optical emission (Shakura & Sunyaev 1973; Netzer 2013). By contrast, disks around stellar-mass black holes reach much higher temperatures (up to a few $\times 10^6$ K), and therefore emit mostly in X-rays (Shakura & Sunyaev 1973; Netzer 2013). Due to the radial temperature gradient, the emitted spectrum cannot be described as a single blackbody. Instead, it results

from a superposition of many blackbody-like components at different temperatures, often referred to as a multicolour black-body (Netzer 2013). This produces a broad optical–UV continuum of ionizing photons, which interact with gas clouds near the nucleus and play a crucial role in shaping the spectral features of the broad-line and narrow-line region. These photons cause photoionization followed by recombination, which gives rise to the strong emission lines that are characteristic of AGN spectra (Netzer 2013).

Broad-Line and Narrow-Line Region

The ionized line-emitting gas clouds can be divided into the broad-line region (BLR) and the narrow-line region (NLR). Both regions differ in density, distance from the SMBH, and the observed line widths (Urry & Padovani 1995). The BLR is located close to the nucleus, at distances ranging from a few light-days to a few light-years from the central SMBH (Goad et al. 2012; see Figure 2.1). It consists of dense gas clouds with electron densities of $n_e \approx 10^{11}\,\mathrm{cm^{-3}}$, moving at velocities of several thousand $\mathrm{km\,s^{-1}}$ due to the strong gravitational influence of the SMBH. These velocities lead to significant Doppler broadening of permitted emission lines, with widths of $(500\text{--}10.000)\,\mathrm{km\,s^{-1}}$ (Peterson 1997). As described earlier, the BLR is photoionized by the continuum radiation emitted from the accretion disk. Consequently, the line emission from this region responds to changes in the continuum, leading to a strong correlation between the two, and strong variability (Netzer 2013). This relationship is particularly relevant for reverberation mapping, which will be discussed later in Section 2.2.

Modeling the geometry of the BLR is challenging because several emission lines have to be considered and their intensities vary in response to changes in the continuum radiation (Netzer 2013). A current basic concept locates the BLR just above the accretion disc, between the disc's edge and the dusty torus (Gaskell 2009; Goad et al. 2012), with inflowing and outflowing gas (Czerny & Hryniewicz 2011) and a disc-like distribution (e.g. Williams et al. 2018). It also shows radial ionization stratification (Collin-Souffrin & Lasota 1988; Gaskell & Sparke 1986; Kollatschny et al. 2001), with higher-ionization lines found closer to the SMBH than lower-ionization lines. Typical broad emission lines include the Balmer, Lyman, and helium lines (Netzer 2013).

The narrow-line region (NLR) extends out to several hundred parsecs from the central region (Peterson 1997). The gas in this region moves at much lower velocities, resulting in emission lines with widths typically of order $(350\text{--}400)\,\mathrm{km\,s^{-1}}$

(Peterson 1997). In contrast to the BLR, the NLR exhibits both permitted and forbidden transitions. Forbidden lines, such as [O III] $\lambda5007$, are prominent in the NLR because at its low densities ($n_e \sim 10^2$–$10^4\,\mathrm{cm^{-3}}$) collisional de-excitation is rare, allowing radiative decay from metastable levels (Peterson 1997). Due to its much larger extent compared to the BLR, the NLR responds only very slowly to variations in the ionizing continuum. Therefore, the flux of the narrow emission lines can be treated as constant over timescales of several years (Peterson 1993).

Because permitted emission lines can originate in both the BLR and the NLR, they often exhibit a multi-component line profile consisting of a broad and a narrow component (Peterson 1997). The relative strength of the broad and narrow components depends on the fractional contribution of emission from the BLR and the NLR, respectively (Peterson 1997).

Dusty Torus

Surrounding the accretion disk and the broad-line region is the dusty torus, a geometrically thick, optically dense structure composed of gas and dust. It extends from the radius at which dust can survive the intense radiation from the accretion disk out to scales of a few parsecs (Netzer 2013). The torus likely has a clumpy distribution and plays a crucial role in the unified model of AGNs (Urry & Padovani 1995; Netzer 2013). The dust in the torus absorbs a significant fraction of the UV and optical radiation emitted by the accretion disk and re-emits it thermally in the infrared. As a result, AGNs typically exhibit strong infrared emission, with the peak wavelength depending on the dust temperature in the torus (Netzer 2013). Even when the central region is hidden from direct view by the torus, this reprocessed infrared emission remains observable. It therefore provides a characteristic signature of obscured AGN activity and enables indirect constraints on the otherwise hidden central engine (Netzer 2013).

2.1.2 Classification

AGNs are classified into subgroups based on their spectral features. The key parameters for this classification are luminosity, emission-line profiles and radio properties. Based on those parameters AGNs get grouped into Seyfert galaxies, quasars and radio galaxies (Peterson 1997). Seyfert galaxies are further subdivided, based on the presence of broad and narrow emission lines (Peterson 1997), as discussed in the following section. Examples of other subclasses are narrow-line Seyfert 1 galaxies
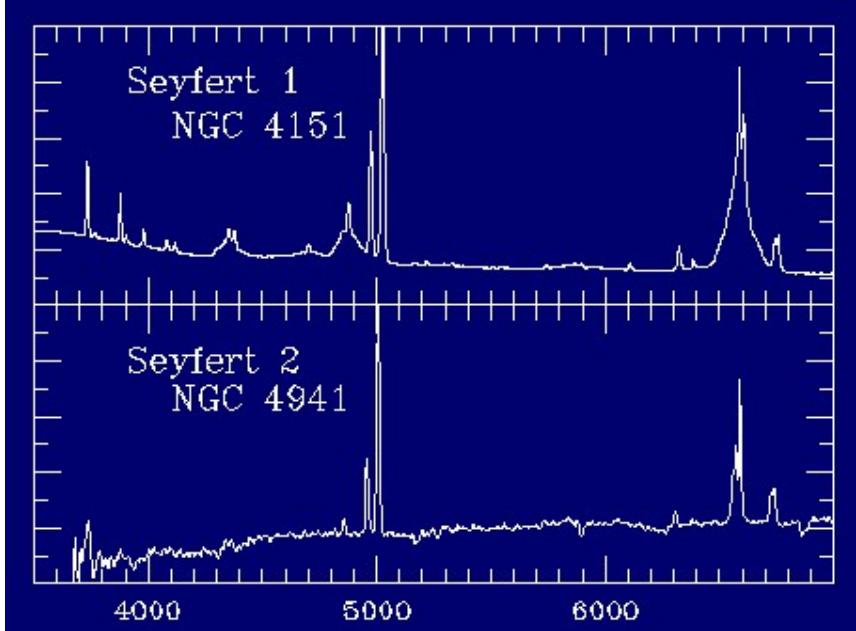
Figure 2.2: An example of Seyfert I and Seyfert II spectra illustrating their differences. Broad lines, such as $H\alpha$ and $H\beta$, are only present in the Seyfert I spectrum, whereas forbidden [O III] lines are visible in both cases. Adapted from Keel 2002.

(NLS1s), low-ionization nuclear emission-line regions (LINERs), and jet-dominated sources such as BL Lac objects or blazars (Antonucci 1993; Urry & Padovani 1995).

Seyfert Galaxies

Seyfert galaxies are named after Carl K. Seyfert, who in 1943 observed spiral galaxies characterized by exceptionally bright nuclei and strong emission lines in their optical spectra (Seyfert 1943). They are classified into the sub-classes Seyfert I and Seyfert II based on the presence of broad emission lines (Peterson 1997), which is demonstrated in Figure 2.2.

Seyfert I galaxies, show both broad and narrow emission lines in their optical spectra. Broad lines (e.g the Balmer line Hα) typically exhibit full widths at half maximum (FWHM) of several thousand kilometers per second and emerge from the fast-moving, high-density gas in the BLR (Peterson 1997). In contrast, narrow lines, including prominent forbidden transitions like [O III] $\lambda5007$ or [N II] $\lambda6584$, originate from the slow-moving, low-density gas in the NLR (Peterson 1997). An AGN showing both components in its spectrum is classified as a Seyfert I galaxy (Peterson 1997), as is the case which is the case for NGC 4593. Further details on NGC 4593 are provided in Section 3.1. Between the two main Seyfert classes, several intermediate subclasses (1.2, 1.5, 1.8, 1.9) are defined based on the relative strength of the broad and narrow Balmer-line components in the optical spectrum

(Osterbrock 1977; Osterbrock 1981; Peterson 1997). Seyfert 1.8 and 1.9 galaxies show very weak broad components. In Seyfert 1.9 objects, the broad component is visible only in the Hα line, whereas in Seyfert 1.8 objects it is also detectable in Hβ. Furthermore, if the broad and narrow components in Hβ are of equal strength, the AGN is classified as a Seyfert 1.5 (Peterson 1997). If the narrow component is even weaker than the broad component, it is classified as a Seyfert 1.2 (Osterbrock 1977).

Seyfert II galaxies lack broad-line emission in their optical spectra, most likely due to orientation-dependent obscuration by a dusty torus (Antonucci 1993; Peterson 1997).This implies that the classification of Seyfert galaxies depends strongly on the observer's viewing angle, which is a central element of the unified model of AGN (Antonucci 1993; Peterson 1997). The unified model is discussed in more detail in Section 2.1.3.

Another notable subclass of Seyfert galaxies is narrow-line Seyfert I galaxies (NLS1s). They are commonly defined by the comparatively small width of the typically broad Hβ emission line (FWHM $< 2000\,\mathrm{km\,s^{-1}}$) and weak [O,III] $\lambda 5007$ emission relative to Hβ (Osterbrock & Pogge 1985; Komossa 2007), and they typically show strong Fe II emission (Véron-Cetty et al. 2001). Strong Fe II emission often correlates with weak [O III] emission and small Balmer-line widths, which provides strong constraints on the physical properties of the central region of an AGN and makes NLS1s of particular interest for study (Osterbrock & Pogge 1985; Komossa 2007).

Additional AGN Classes

In addition to Seyfert galaxies, there are several other classes of AGNs. Quasars (quasi-stellar objects) are more luminous than Seyfert galaxies, typically outshine their host galaxies, and are usually observed at higher redshifts (Netzer 2013). Because quasars show emission properties identical to those of Seyfert galaxies, the modern distinction is primarily based on luminosity: quasars are high-luminosity AGNs, whereas Seyfert galaxies occupy the lower-luminosity end (Netzer 2013).

Radio galaxies form another important AGN class, distinguished by their strong radio emission and prominent jets and are typically found in elliptical host galaxies (Netzer 2013). When their jets are aligned close to the observers line of sight, they are observed as blazars or BL Lac objects, which exhibit rapid variability and featureless optical spectra due to relativistic beaming (Netzer 2013).

Finally, LINERs are low-luminosity AGNs with spectra dominated by low-ionization emission lines. The physical origin of their ionization mechanism is still debated,

and in some cases, they may not be powered by accretion at all (Netzer 2013). While these classifications are based primarily on spectral characteristics, many of the observed differences between AGN types can be attributed to orientation effects. The Unified Model of AGN provides a framework that explains this apparent diversity through a common internal structure, viewed from different angles.

2.1.3 Unification Model

Figure 2.3 illustrates the unified model of AGN proposed by Antonucci 1993. He argued that the observed differences among AGN spectra do not require fundamentally different intrinsic structures. Instead, they arise mainly from orientation of the central region towards the observer and from its obscuration by the dusty torus.

The figure shows how the same AGN would be classified depending on the observer's viewing angle. As mentioned above, the dusty torus plays a key role, as it surrounds the SMBH, the accretion disk and the fast-moving BLR. If the line of sight is blocked by the torus, the broad-line emission is obscured, resulting in a Seyfert II spectrum, exhibiting only narrow emission lines. In this geometry, the AGN is viewed at high inclination, with the torus intercepting the line of sight. If, on the other hand, the nucleus is viewed directly and is not obscured by the torus, both broad and narrow emission lines are observed in the spectrum, and the AGN is classified as a Seyfert I galaxy (Urry & Padovani 1995).

The same principle applies to other AGN classes. Quasars can be considered the high-luminosity counterparts of Seyfert galaxies, where orientation and torus obscuration likewise affect their observed properties. Blazars, are seen when the relativistic jet is aligned closely with the observer's line of sight, leading to strong Doppler boosting, which makes the radiation appear significantly brighter and shifted to higher frequencies than it intrinsically is (Urry & Padovani 1995).

Although the classical Unification Model treats AGN classification as fixed and purely geometry-driven, some AGNs have been observed to change their spectral type over time (e.g. Ricci & Trakhtenbrot 2023). These so-called "changing-look AGNs" demonstrate that a purely orientation-based interpretation, such as the Unification Model, cannot explain all observed phenomena. They suggest that intrinsic changes, such as variations in accretion rate or obscuring material, can also affect the classification (Ricci & Trakhtenbrot 2023).
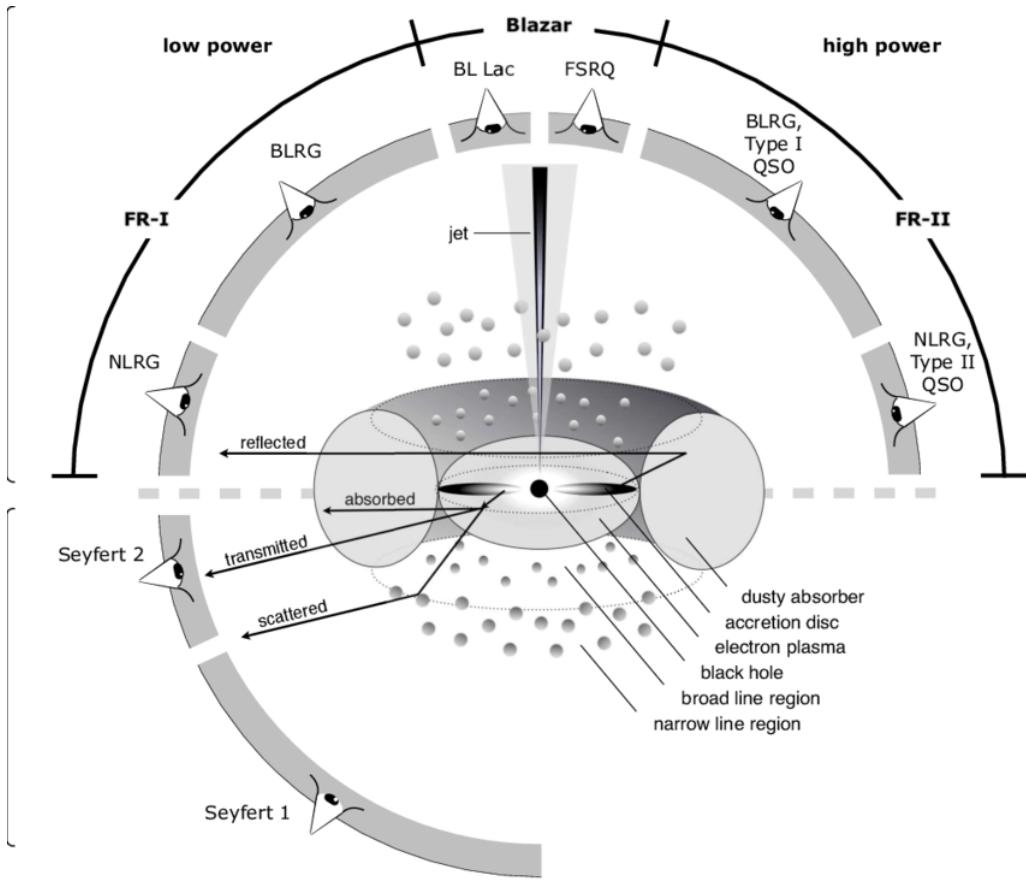
Figure 2.3: This graphic shows a schematic of the unification model of an AGN. The figure was adopted from Beckmann & Shrader 2013.

2.1.4 Variability

The variability of active galactic nuclei is one of the key aspects that enables the study of their central regions, which generally cannot be probed with conventional spatially resolved observations. Variability is observed on timescales ranging from hours to several years and is generally stochastic, resulting in flux variations of both emission lines and continuum emission of up to a few tens of percent in the UV and optical bands (Ulrich et al. 1997). Although the origin of this variability is not yet fully understood, the most widely accepted models attribute it to inhomogeneities and instabilities within the accretion disk (Ulrich et al. 1997; Dexter & Agol 2010). Depending on the underlying physical process, variations occur on different characteristic timescales. Processes such as thermal fluctuations or changes in the accretion flow happen on timescales of decades to centuries for typical SMBH masses and radii, and are therefore difficult to observe directly. In contrast, processes operating on shorter timescales are easier to study. Examples include gas motions and mechanical instabilities (e.g., sound waves) within the disk, which occur on timescales of weeks

to months (Ricci & Trakhtenbrot 2023). The shortest timescale is the light-crossing timescale, $t_{\mathrm{lc}} = R/c$, which specifies how long light takes to traverse the emitting region (e.g. BLR) (Ricci & Trakhtenbrot 2023). Here, c denotes the speed of light, and R denotes the characteristic size or radius of the variable emitting region. Following Ricci & Trakhtenbrot 2023, assuming a SMBH of mass $\approx 10^8 \, M_\odot$, the light-crossing timescale can be written as

$$t_{\mathrm{lc}} = \frac{R}{c} \simeq 0.87 \left(\frac{R}{150 \, r_g} \right) M_8 \, \mathrm{days}, \tag{2.1}$$

where $r_g = GM/c^2$ is the gravitational radius of the black hole. Thus, the light-crossing timescale of the variable emitting region is of order days, and t_{lc} scales linearly with the size of the emitting region (Ricci & Trakhtenbrot 2023).

Because variations in the ionizing continuum occur on such short timescales, it is possible to measure delayed responses from other regions within the AGN that are correlated with the continuum, using long-term monitoring campaigns (Peterson 1997). In particular, the BLR responds to changes in the photoionizing continuum radiation of the central source with a time delay (lag) that is longer than the light-crossing timescale of the emitting region (Peterson 1997). This lag forms the basis of classical reverberation mapping, which will be further elaborated in the next section.

2.2   Reverberation Mapping

The main focus of this work is a classical reverberation mapping analysis of the broad lines of NGC 4593. Reverberation mapping probes the structure of the BLR around the SMBH by measuring the time delay (lag) between continuum variations and the correlated response of the broad lines. This lag can be used to constrain the BLR geometry and to estimate the SMBH mass (Peterson 1993).

2.2.1   Principle of Reverberation Mapping

The fundamental assumption in reverberation mapping is that variations in the observed continuum flux are echoed by variations in the emission-line flux, with a measurable time delay (lag). When the continuum luminosity varies, the emission-line response follows with a measurable time lag (Peterson 1993). The time lag τ corresponds to the average light-travel time between the photo-ionizing continuum source and the line-emitting regions. Following the derivation of Peterson 1997, τ can be written as

$$\tau = (1 + \cos\theta) \cdot \frac{R_{\mathrm{BLR}}}{c}, \tag{2.2}$$

Figure 2.4: Spherical BLR model and an isodelay surface, adopted from (Peterson & Horne 2004).

where R_{BLR} is the characteristic BLR radius, c is the speed of light, and θ is the angle between the line of sight and the position vector of the emitting gas with respect to the central source (see Figure 2.4; Peterson 1997). The circle in Figure 2.4 represents the BLR modeled as spherical distribution of the clouds. For a fixed lag τ, the emitting regions that respond at that delay lie on a paraboloid aligned with the observer's line of sight, known as an isodelay surface. Therefore, emission observed at a given lag τ originates from the intersection of the BLR distribution with the corresponding isodelay surface (Peterson 1997). Thus, reverberation mapping can be used to "map" the BLR by inferring a characteristic BLR radius from the measured time lag (Peterson 1997). However, the observer receives emission from a range of delays (i.e., effectively from many isodelay surfaces), so the so-called transfer equation is required, which integrates over all delays (Peterson 1997):

$$L\left(t\right) = \int \Psi\left(\tau\right) C\left(t - \tau\right) d\tau. \tag{2.3}$$

Here, $\Psi(\tau)$ is the transfer function, which encodes the BLR geometry and kinematics, $C(t)$ is the continuum light curve, and $L(t)$ is the emission-line light curve (Peterson 1997). Although the BLR response is, in principle, fully described by the transfer function $\Psi(\tau)$, the lag is commonly estimated using cross-correlation techniques. In practice, recovering the full transfer function $\Psi\left(\tau\right)$ requires densely sampled, high signal-to-noise light curves spanning a duration much longer than the expected lag. Since real monitoring campaigns are often affected by observational gaps and noise, such reconstructions are rarely possible (Horne et al. 2004; Peterson 1993). For this reason, this project focuses on measuring the mean time lag between continuum and emission-line variations using the interpolated cross-correlation function (ICCF) method (Gaskell & Peterson 1987), which is well established in RM cam-

17

paigns (e.g. Kollatschny & Dietrich 1997; Denney et al. 2006; Williams et al. 2018; Probst et al. 2025).

2.2.2 Lag Measurement

Using the notation of Peterson 1997, the cross-correlation function between the ionizing continuum and an emission line is defined as

$$F_{\mathrm{CCF}}(\tau) = \int_{-\infty}^{\infty} L(t)C(t-\tau)dt. \tag{2.4}$$

The auto-correlation function of the ionizing continuum is

$$F_{\mathrm{ACF}}(\tau) = \int_{-\infty}^{\infty} C(t)C(t-\tau)dt. \tag{2.5}$$

Together with the transfer equation (Equation 2.3), the cross-correlation function can be written as the convolution of the transfer function and the auto-correlation function of the ionizing continuum:

$$F_{\mathrm{CCF}}(\tau) = \int_{-\infty}^{\infty} \Psi(\tau')F_{\mathrm{ACF}}(\tau-\tau')d\tau'. \tag{2.6}$$

The lag is commonly defined as either the peak location (τ_{peak}) or the centroid (τ_{centroid}) of the CCF (Peterson 1997). While τ_{peak} is defined as the location of the CCF maximum, τ_{centroid} is calculated over all CCF points above a selected threshold, typically 80% of the peak value. Because the CCF is closely related to the transfer function, it is possible to infer a characteristic BLR size associated with the emission-line response (Peterson 1997), which can be expressed as

$$R_{\mathrm{BLR}} = c \cdot \tau_{\mathrm{centroid}}. \tag{2.7}$$

This follows from the light-travel timescale (Peterson et al. 2004). Since the centroid lag is generally considered a more robust estimator of the mean BLR light-travel time of the BLR (Peterson et al. 2004), it is used in this project.

The uncertainty of the measured lag is estimated using a Monte Carlo approach combining flux randomization (FR) and random subset selection (RSS) (Peterson et al. 1998; Peterson et al. 2004). In the FR step, each flux value is randomly perturbed according to its measurement uncertainty. In the RSS step, N data points are drawn randomly with replacement, while duplicate selections are discarded, resulting in a new light curve with $M \leq N$ points. For each realization, the ICCF analysis is

repeated, yielding a distribution of centroid lags. The uncertainties are estimated from the distribution of centroid lags obtained from the simulations (Peterson et al. 2004). The 16th and 84th percentiles of this distribution are adopted as the bounds of the 1σ confidence interval (Peterson et al. 1998).

2.2.3 Black Hole Mass

The reverberation mapping method can be used not only to measure the characteristic size of the BLR, but also to estimate the mass of the central SMBH. Under the assumption that the gas dynamics in the BLR are dominated by the gravitational potential of the central SMBH, the black hole mass can be estimated using the virial theorem (Peterson et al. 2004).

The centroid time lag τ_{centroid} provides an estimate of the characteristic BLR radius via Equation 2.7. Together with the velocity dispersion ΔV of the BLR gas, the virial mass is given by

$$M_{\mathrm{vir}} = \frac{R_{\mathrm{BLR}}\,\Delta V^2}{G}. \tag{2.8}$$

The black hole mass is then given by

$$M_{\mathrm{BH}} = f \cdot M_{\mathrm{vir}}. \tag{2.9}$$

Here, G denotes the gravitational constant, and f is a scale factor that accounts for the unknown geometry, kinematics, and inclination of the BLR (Peterson et al. 2004). The velocity dispersion ΔV can be estimated from the widths of the broad emission lines (Peterson et al. 2004).

The scale factor f is calibrated by matching reverberation-based black hole masses to the empirical $M_{\mathrm{BH}} - \sigma_*$ relation observed in inactive galaxies, where σ_* denotes the stellar velocity dispersion of the galactic bulge (Onken et al. 2004). Different studies have reported values of f based on various AGN samples, for example, $f = 5.5$ (Onken et al. 2004), $f = 4.31$ (Grier et al. 2013), and $f = 3.6$ (Graham et al. 2011). The calibration of the scale factor also depends on the measurement method used for the line width of the broad emission lines (Peterson et al. 2004). Two commonly used measures are the line dispersion σ_{line} (see Peterson et al. 2004) and the FWHM. As this work focuses on the FWHM measures and the previously named scale factories where estimated with the line dispersion measure, a average scale factor of $f = 1.8$ gets adopted, following Probst et al. 2025. This value bases on the average scale factor $f = 3.6$ reported by Graham et al. 2011 and takes the relation $\mathrm{FWHM}/\sigma_{\mathrm{line}} \approx 2$ Peterson et al. 2004 into account.

2.3 Bowen Fluorescence of OIλ8446

Previous studies of NGC 4593 report strong emission in the low-ionization lines
O I λ8446 and the Ca II λ8498 λ8542 λ8662 triplet (Ochmann et al. 2025). In particular, O I λ8446 is of interest because it can be enhanced through a fluorescence
mechanism referred to as Bowen fluorescence (Bowen 1947; Grandi 1980). The mechanism was first described by I.S. Bowen in 1934 to explain unexpected emission lines
in nebular spectra. This mechanism describes a resonant line-pumping process in
which photons emitted by one ion are absorbed by another ion of a different species
via a permitted transition enabled by a near coincidence in wavelength between the
pumping line and the absorbing transition. The resulting de-excitation leads to an
enhancement of the emission lines (Bowen 1934).

One transition that can be enhanced by Bowen fluorescence is O I λ8446, which
can be pumped by Lyβ photons (Bowen 1947; Netzer & Penston 1976). In this
process, Lyβ photons at λ1025.72 Å are absorbed by neutral oxygen through the
near-resonant transition $2p^4\,^3P_2 \rightarrow 3d\,^3D^0$ of O I at λ1025.77 Å. The excited $3d\,^3D^0$
level decays to $3p\,^3P$, which then decays to $3s\,^3S°$, emitting the O I λ8446 emission
line (see Figure 2.5; Grandi 1980). This provides an additional excitation channel
for O I λ8446, in addition to recombination, continuum fluorescence or collisional
excitation.
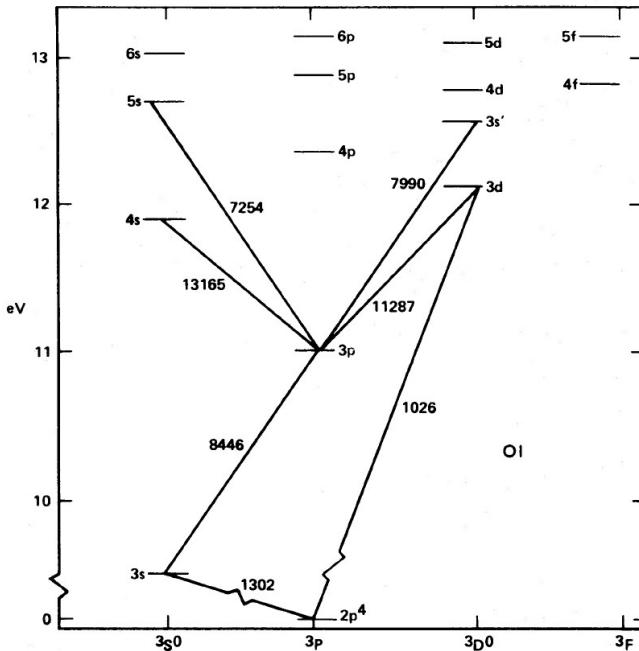
Figure 2.5: Energy level diagram displaying the process of Bowen fluorescence pumping of OI, adopted from (Grandi 1980).

3. Campaign and Data Preparation

The analysis of this campaign is based on the HST dataset of the observation campaign of NGC 4503 in 2016 (PI: Cackett, E.M, Prop ID 14121). This campaign took place between the 12th of July and the 6th of August with daily observations, which resulted in 26 successful out of 27 observations. It was performed with the Hubble Space Telescope (HST) using the Space Telescope Imaging Spectrograph (STIS) with the three different Gratings. The following section will cover an overview of the properties and specifications of NGC4593 and the campaign in 2016.

3.1 NGC4593

NGC 4593 is classified as a Seyfert 1 galaxy with a barred spiral morphology of type (R)SB(rs)b (Denney et al. 2006). It is located at RA = $12^\mathrm{h}39^\mathrm{m}39.44^\mathrm{s}$, Dec = $-05°20'39.03''$ (J2000) and has a redshift of $z = 0.0083 \pm 0.0005$, corresponding to a distance of $\sim 35.9\,\mathrm{Mpc}$ (NED 2025) assuming a ΛCDM cosmology. The galaxy exhibits a prominent large-scale bar and nuclear dust ring connected to dust lanes along the bar, as seen in Figure 3.1.

The AGN in NGC 4593 exhibits strong broad emission lines, including Balmer and Lyman lines as well as He, O, and Ca lines among others (Kollatschny & Dietrich 1997; Denney et al. 2006; Cackett et al. 2018; Ochmann et al. 2025). Several variability and reverberation-mapping campaigns have monitored different broad emission lines(e.g. Dietrich et al. 1994; Kollatschny & Dietrich 1997; Denney et al. 2006. They reported FWHM values from the mean (AVG) and root-mean-square (RMS) spectra of their respective campaigns. The RMS spectrum is defined as the standard deviation of the flux at each wavelength across epochs:

$$F_{\mathrm{RMS}}(\lambda) = \sqrt{\frac{1}{N-1} \sum_{i=1}^{N} \left[F_i(\lambda) - \bar{F}(\lambda) \right]^2}, \qquad (3.1)$$
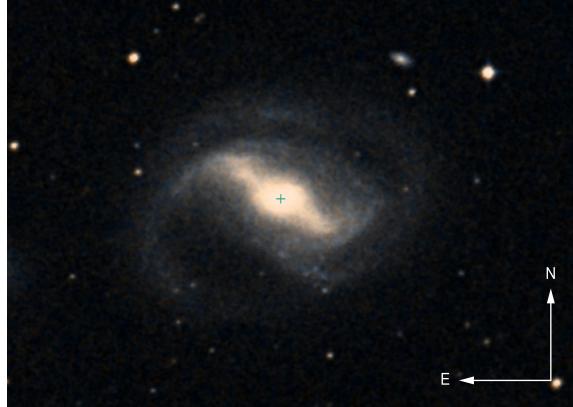
Figure 3.1: Screenshot of NGC 4593 visualized with Aladin Lite (*Aladin Lite* 2025) using DSS2 survey imagery (STScI 2025). The image is oriented with north up and east to the left. Right ascension increases to the left and declination increases upward.

with the mean spectrum at wavelength λ given by

$$\bar{F}(\lambda) = \frac{1}{N} \sum_{i=1}^{N} F_i(\lambda) \,. \tag{3.2}$$

Kollatschny & Dietrich 1997 measured $\text{FWHM}_{\text{AVG/RMS}} = (3400 \pm 200)\,\text{km s}^{-1}$ for Hα, while Denney et al. 2006 reported for Hβ $\text{FWHM}_{\text{AVG}} = (5142 \pm 16)\,\text{km s}^{-1}$ and $\text{FWHM}_{\text{RMS}} = (4141 \pm 416)\,\text{km s}^{-1}$. Based on these broad-line widths, they estimated the SMBH mass to be $M \approx 1.4 \times 10^7\,M_\odot$ (Kollatschny & Dietrich 1997) and $M = (9.8 \pm 2.1) \times 10^6\,M_\odot$ (Denney et al. 2006). Overall, these results suggest that the SMBH mass is of order $10^7\,M_\odot$.

Furthermore, NGC 4593 shows a rare double-peaked emission-line complex involving O I λ8446 and the Ca II λ8498, λ8542, λ8662 triplet (Ochmann et al. 2025). Ochmann et al. 2025 found that the Ca II triplet has an intensity ratio of 1:1:1 and line profiles that closely resemble those of O I λ8446, exhibiting a red-to-blue peak ratio of 4:3 and a FWHM of $\approx 3700\,\text{km s}^{-1}$, suggesting that these lines originate in a similar high-density emission region. A fit of the asymmetric line profile of Ca II λ8662 with an elliptic accretion disk model, shows an eccentric of $e \approx 0.22$ and a low-inclination of $i \approx 11°$.

3.2   The 2016 HST Campaign

The HST campaign (PI: Cackett, E.M, Prop ID 14121) was designed to study wavelength-dependent continuum lags. It took place between the 12th of July and the 6th of August with daily observations, which resulted in 26 successful out of 27

observations. Observations were carried out with the Hubble Space Telescope (HST) using the Space Telescope Imaging Spectrograph (STIS) and three different gratings. The low-resolution STIS gratings provided continuous spectral coverage over a broad wavelength range of approximately $1100\,\text{Å} - 1700\,\text{Å}$ and $3900\,\text{Å} - 9000\,\text{Å}$. In each observation, spectra were obtained using the G140L, G430L, and G750L. All spectra were acquired with the $52'' \times 0.2''$ slit.

The characteristics of the STIS gratings used in this work are summarized in Table 3.1. After standard pipeline processing, charge-transfer inefficiency (CTI) corrections were applied using an algorithm based on (Anderson & Bedin 2010). The remaining hot pixels were removed manually by M. Ochmann.

We retrieved 27 spectra from the *Hubble Advanced Spectral Products (HASP)* 2025 archive using the HASP search form in *Mikulski Archive for Space Telescopes (MAST)* 2025. 26 of these spectra are usable for further analysis. The top panel of Figure 3.2 shows all spectra in the spectral range from 4000Å to 9000Å.

Table 3.1: Overview of STIS grating characteristics (STIS 2025).

Grating	Range [Å]	Exp. Time [s]	Res. Power	Dispersion [Å/pixel]
G140L	1119–1715	1234	~ 1000	0.6
G430L	2888–5697	298	$\sim 500 - 1000$	2.73
G750L	5245–10233	288	$\sim 500 - 1000$	4.92

3.3 Intercalibration and Determination of AVG and RMS Spectra

For the subsequent analysis, the average spectrum (AVG) is obtained by averaging over all epochs, improving the signal-to-noise ratio (S/N). Furthermore it is essential for the reverberation mapping analysis to identify variability between the epochs, which can be assessed with the root-mean-spuare (RMS) spectrum, defined as the standard deviation of the flux at each wavelength across epochs (see. Equation 3.1). Constant features, such as narrow emission lines, vanish in the RMS spectrum, leaving only variable components such as broad emission lines. The top panel of Figure 3.2 shows the AVG and RMS spectra from the original retrieved data. Residual variability is still noticeable in nominally non-varying lines, particularly in the forbidden line [O III] $\lambda5007$. This indicates small wavelength misalignment between epochs. Therefore, an intercalibration anchored to the narrow [O III] $\lambda5007$ line was performed, which is common practice in RM campaign (e.g. Dietrich et al. 1994;

Denney et al. 2006). This was achieved by shifting the wavelengths of the individual spectra and scaling the [O III] $\lambda5007$ line flux to a constant value. As a narrow line, the flux of [O III] $\lambda5007$ can be assumed to remain constant over the timescale of the campaign. Based on this assumption, the [O III] flux in each spectrum was scaled to $(106 \pm 5) \times 10^{-15}\,\mathrm{erg\,s^{-1}\,cm^{-2}}$ and the wavelength was shifted by a maximum of 1Å.

Figures 3.2 shows a comparison of the original and the intercalibrated epochs and the corresponding AVG and RMS spectra. The disappearance of narrow features in the calibrated RMS spectrum, especially the [O III] $\lambda5007$ line, confirms that the apparent variability in the RMS of the original epochs was induced by the wavelength shifts between them, rather than intrinsic line variability. However the intercalibration was only applied to the optical part of the spectra, because a narrow-line flux calibration is only valid over a limited wavelength regime. In the following analysis, the intercalibrated AVG and RMS spectra are used for the optical range obtained with the G430L and G750L gratings, while the AVG and RMS spectra from the original epochs are used for the UV emission-line analysis, as these were acquired with the G140L grating.

Figure 3.2: Comparison of the spectral range between 4000Å and 9000Å from the 2016 HST campaign of NGC 4593, showing the effects of [O III] $\lambda5007$ intercalibration on both the individual spectra (top) and the derived average and rms spectra (bottom).

4. Reverberation Mapping Analysis of NGC4593

4.1 Line Identification

To begin the RM analysis, the emission lines in the AVG spectrum are identified. This is done for the optical–NIR range $3900\,\text{Å}$–$9000\,\text{Å}$ and for the UV range $1100\,\text{Å}$–$1700\,\text{Å}$.

In the optical–NIR range (see Figure 4.1), several prominent broad emission lines are identified: Balmer lines from $H\alpha$ – $H\epsilon$; He I $\lambda4471$, He I $\lambda5016$, He I $\lambda5876$ and He I $\lambda7065$; He II $\lambda4686$; and the low-ionization lines O I $\lambda8446$ and the Ca II $\lambda8498$ $\lambda8542$ $\lambda8662$ triplet. All of these lines show some level of variability in the RMS spectrum. For the subsequent analysis, the Balmer lines $H\alpha$ – $H\delta$, He II $\lambda4686$ and He I $\lambda5876$ are selected for the subsequent analysis, as they show the most pronounced variation in the RMS spectrum. The low-ionization line O I $\lambda8446$ shows noticeable variability, which was not monitored in a RM analysis yet and is therefore included as well. Two prominent Fe II emission line bands are also present in the optical spectrum as well, one between $\sim 4489\,\text{Å} - 4629\,\text{Å}$, blending with He I $\lambda4471$ and He II $\lambda4686$, and another between $\sim 5169\,\text{Å} - 5336\,\text{Å}$. The AVG spectrum also shows several narrow forbidden emission lines, with [O III] $\lambda4363$, $\lambda4959$, and $\lambda5007$ being the most prominent. As they are assumed to be constant over the timescale of the campaign, they show no significant variability in the RMS spectrum.

In the UV spectrum (Figure 4.2), five broad emission lines are identified: Lyα, which overlaps with the N V $\lambda\lambda1238, 1242$ doublet; Si IV $\lambda\lambda1393, 1402$; C IV $\lambda\lambda1548, 1550$; and He II $\lambda1640$. Since the UV emission lines of NGC 4593 were not monitored in a RM analysis yet, these emission lines will be included as well in the subsequent analysis. In addition to the broad emission lines, the UV spectrum exhibits semi-forbidden emission lines, like the O III] $\lambda\lambda 1660, 1666$ doublet, which partially blends with He II $\lambda1640$.
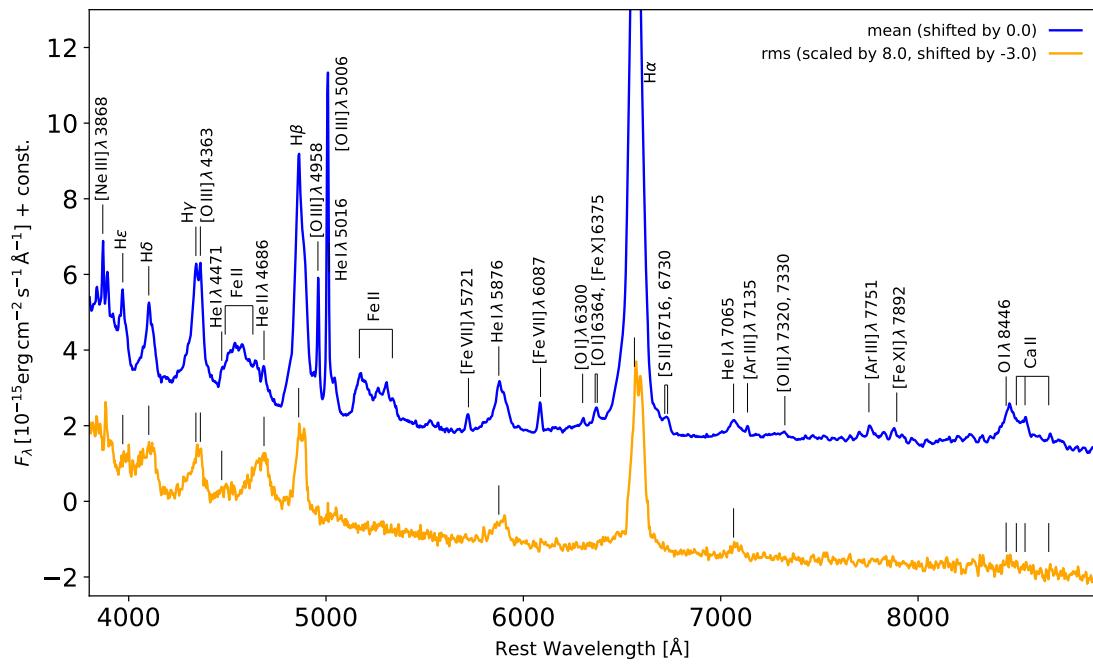
Figure 4.1: Optical-to-NIR AVG and RMS spectrum with identified emission lines.
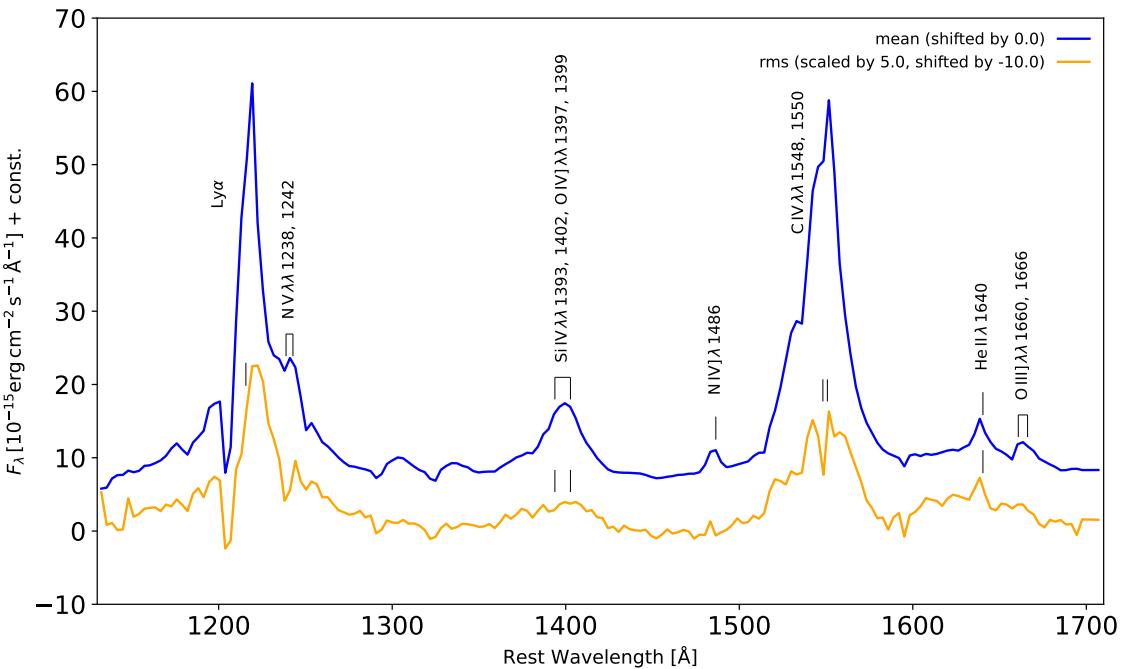
Figure 4.2: UV spectrum AVG and RMS spectrum with identified emission lines

4.2 Emission Line and Continua Measurement

After the identification and selection of the broad emission lines, their fluxes are measured in every epoch to extract their light curves. This is performed with a Python-based tool called GECHO, developed by M. Probst. This tool is able to import full campaigns, determine AVG and RMS spectra, extracting lightcurves and conduct further measurements, naming here line-width measurements and lags measurement based on the methods of Gaskell & Peterson 1987 and Peterson et al. 2004, which are further discussed in Sections 4.5 and 4.4.

The emission line light curve extraction of follows the same principle as in previous RM campaigns (e.g. Kollatschny & Dietrich 1997; Probst et al. 2025). Figure 4.3 shows the GECHO graphical user interface (GUI), which provides a side-by-side view of the campaign's AVG and RMS spectra. The line flux at each epoch is obtained by integrating the flux density over the wavelength range, marked in red in Figure 4.3. The integration boundaries are chosen to include the variable part of the emission line while excluding contributions from neighboring lines. To account for the surrounding continuum, a linear pseudo-continuum is interpolated from two line-free wavelength windows on the blue and red side of the emission line, shown in grey in Figure 4.3. The adopted integration limits and pseudo-continua for each line are listed in Table 4.1.
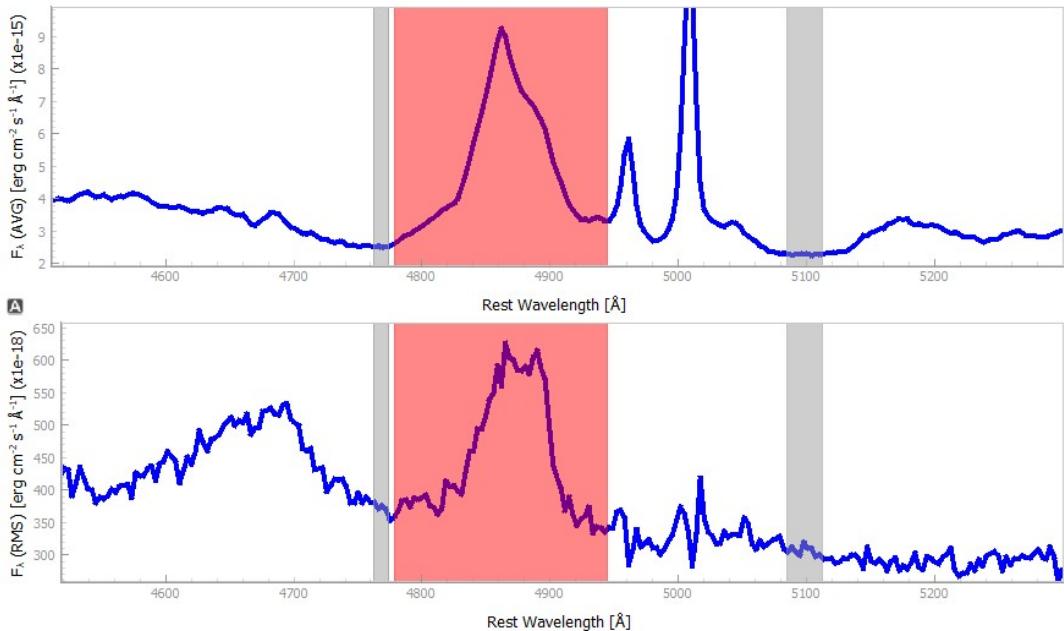
Figure 4.3: Screenshot of the GECHO graphical user interface (GUI). Shown is an example of the selection of the integration boundaries for Hβ and corresponding blue and red pseudo-continuum used to measure the integrated line flux.

The light curves of the continuum emission, that will be used as proxy for the ionizing continuum, are derived from the mean flux density of areas free from line emission. The continuum windows for the light curve extraction of the continuum emission are adopted from Cackett et al. 2018. The wavelength range for the continua are listed in Table 4.2.

Table 4.1: Integration Limits and Pseudo-Continua range of the measured emission lines

Line	Integration Limits [Å]	Pseudo-Continua [Å]
Lyα	$1207 - 1238$	$1151 - 1161, 1461 - 1469$
N v $\lambda\lambda$1238, 1242	$1207 - 1238$	$1151 - 1161, 1461 - 1468$
Si iv $\lambda\lambda$1393, 1402	$1358 - 1423$	$1151 - 1161, 1461 - 1469$
Civ $\lambda\lambda$1548, 1550	$1511 - 1578$	$1461 - 1469, 1680 - 1685$
He ii λ1640	$1599 - 1645$	$1461 - 1468, 1680 - 1685$
Hα	$6453 - 6695$	$6107 - 6129, 6861 - 6900$
Hβ	$4779 - 4944$	$4762 - 4774, 5085 - 5112$
Hγ	$4230 - 4427$	$4197 - 4220, 4435 - 4450$
Hδ	$4035 - 4165$	$4026 - 4033, 4197 - 4220$
He i λ5875	$5742 - 6039$	$5645 - 5653, 6044 - 6057$
He ii λ4685	$4545 - 4758$	$4435 - 4450, 4762 - 4774$
O i λ8446	$8380 - 8500$	$8005 - 8031, 8850 - 8955$
O iii λ5007	$4982 - 5033$	$4762 - 4774, 5085 - 5112$

Table 4.2: Wavelength range of the measured continua

Line	Integration Limits [Å]
Cont. 1150	$1151 - 1161$
Cont. 4010	$4026 - 4033$
Cont. 4440	$4435 - 4450$
Cont. 5100	$5085 - 5112$
Cont. 6110	$6107 - 6129$
Cont. 6880	$6861 - 6900$
Cont. 8015	$8005 - 8031$
Cont. 8900	$8864 - 8955$
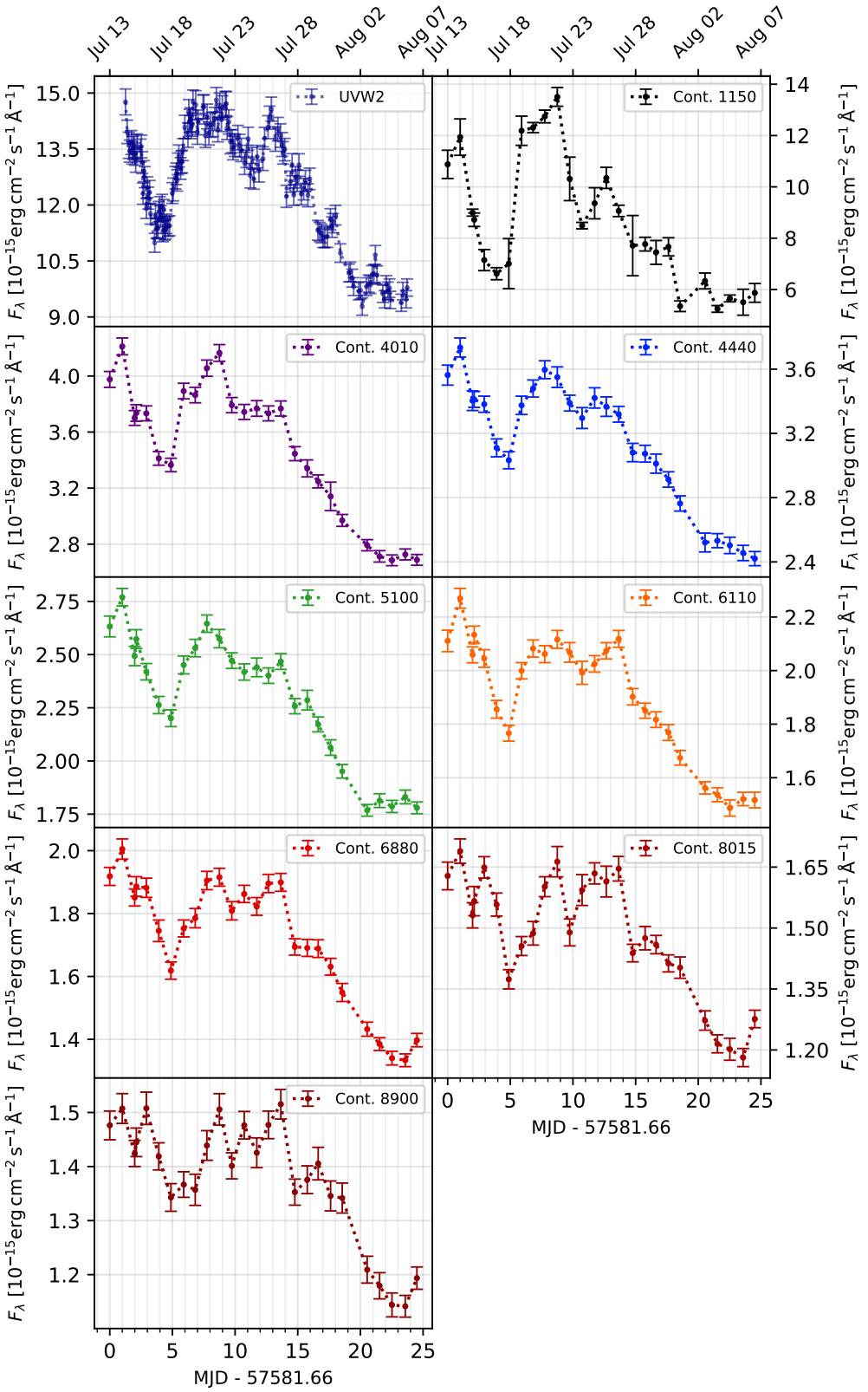
Figure 4.4: Comparison of the continua lightcurves. The first panel shows the photometric *Swift* UVW2 light curve obtained from McHardy et al. 2018, while the other panels show the measured continua defined in Table 4.2
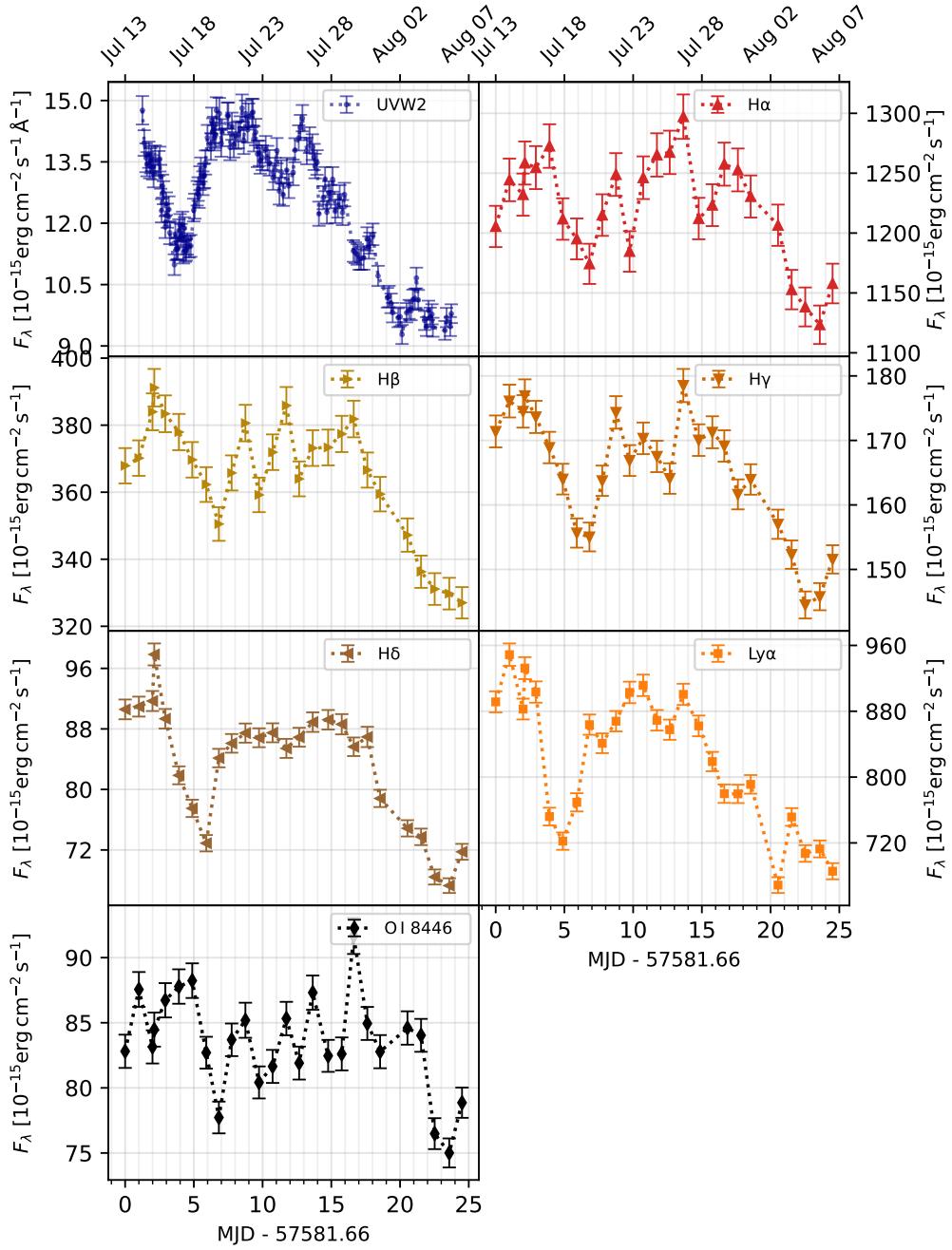
Figure 4.5: Comparison of the Balmer-line, Lyα, and O,ı,λ8446 light curves with the photometric *Swift* UVW2 light curve as reference in the first panel. The *Swift* UVW2 light curve is adopted from McHardy et al. 2018.
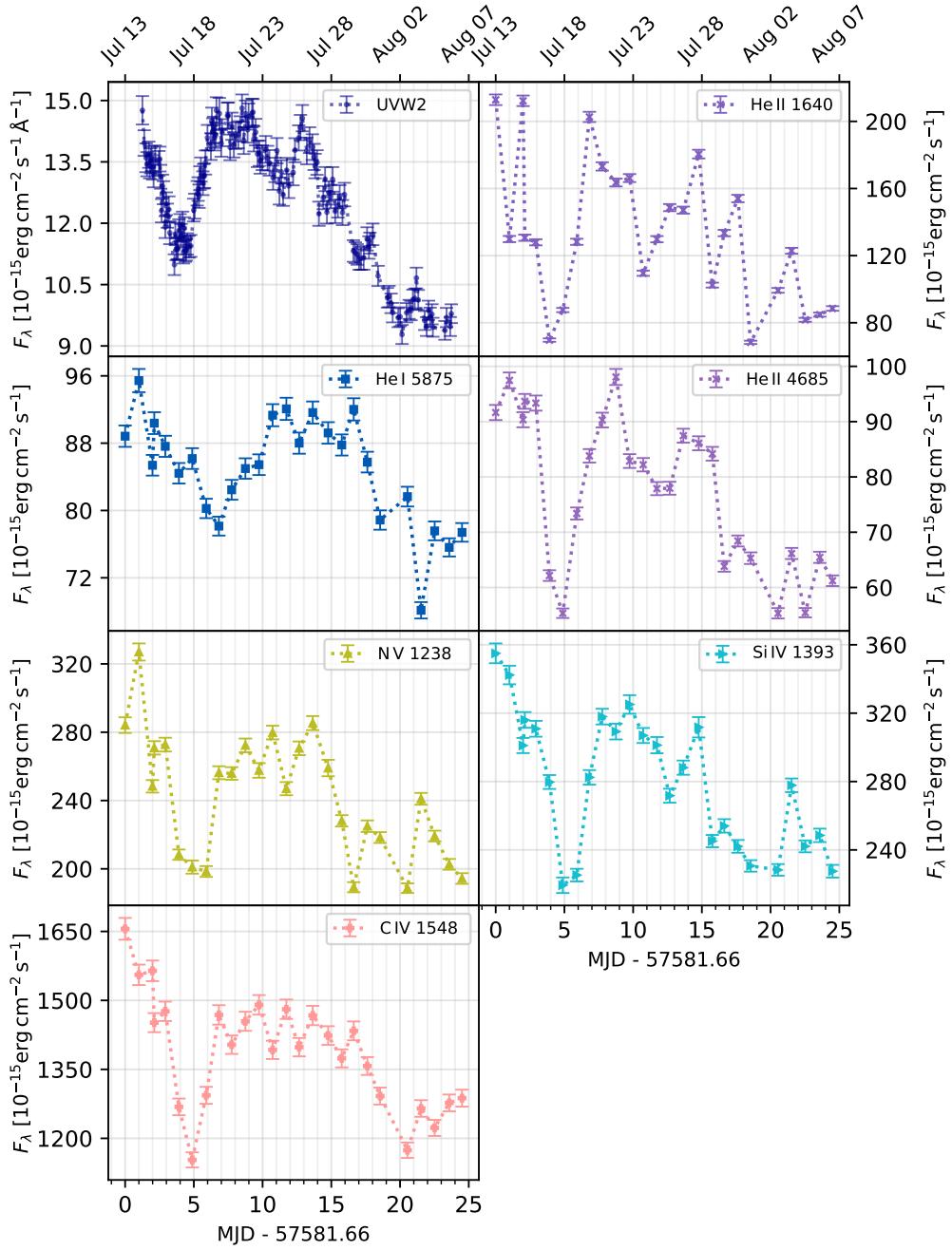
Figure 4.6: Comparison of the Helium and UV light curves with the photometric *Swift* UVW2 light curve as reference in the first panel. The *Swift* UVW2 light curve is adopted from McHardy et al. 2018.

4.3 Lightcurves

Thanks to the covered wavelength range, it was possible to measure several continuum lightcurves in the UV-, optical- and NIR regime. In addition, the photometric UVOT UVW2 lightcurve is included in the subsequent analysis, which was taken with *Swift* and published in McHardy et al. 2018. It has also been used in Cackett et al. 2018 and exhibits a denser sampling than the HST lightcurves, with a cadence of 96 minutes for 6.4 d between July 13 and July 18, 2016 and a central wavelength of about $\sim 1930\,$Å (McHardy et al. 2018).

All continuum lightcurves show a broadly similar shape (see Figure 4.4). The light curves start at high flux and then decrease by about 50–80% relative to their maxima within the first 1–4 days, reaching a minimum between days 4 and 5. Afterwards, the flux increases again in all light curves. The UV continua show a plateau-like behavior from days 6 to 9, followed by a smaller decline between days 9 and 13, before rising again to a peak around day 13. A similar pattern is also noticeable in the other continuum light curves, but becomes less clear at higher wavelengths. While the optical continua also show higher flux levels between days 6 and 9 than between days 9 and 13, the near-IR continua exhibits a plateau over this interval. Towards the end of the campaign, the flux decreases again towards a minimum, with smaller short-term fluctuations, followed by a slight rise in the final days of the campaign in the UV and NIR bands.

The estimation of the physical distance between the SMBH and the region from which the emission lines originate is the main goal of this RM analysis. Assuming that the continuum radiation originates from the accretion disk, it is common to use the bluest available continuum as reference for the time lag estimation, which is expected to originate closest to the SMBH (Peterson 1993). While the bluest continuum is measured around $1150\,$Å in the HST dataset, the UVW2 continuum was selected as the main reference lightcurve for the subsequent analysis due to its higher sampling rate. Therefore, the delay between the continuum light curve around $1150\,$Å and the UVW2 light curve has to be taken into account in the subsequent lag estimation (see. Section 4.4).

Comparing the UVW2 light curve to the measured broad emission line light curves, they exhibit a equally strong decrease in flux, followed by a central part with higher flux and another decrease (see. Figure 4.5 and 4.6). By comparing these features, a correlation of the emission line light curves to the UVW2 light curve is already apparent with a noticeable time lags which is further investigated in Section 4.4.

Table 4.3: Variability statistics of the measured continua and emission lines with minimum flux F_min and maximum flux density or integrated flux F_max, peak-to-peak ratio R_max, mean $\langle F\rangle$, standard deviation σ_F and fractional variation F_var.

Continuum/Line	F_min	F_max	R_max	$\langle F\rangle$	σ_F	F_var
Cont. 1150	0.52	1.35	2.58	0.86	0.25	0.28
Cont. 4010	2.68	4.21	1.57	3.49	0.47	0.14
Cont. 4440	2.42	3.73	1.54	3.14	0.39	0.12
Cont. 5100	1.77	2.77	1.57	2.29	0.3	0.13
Cont. 6110	1.49	2.27	1.53	1.9	0.23	0.12
Cont. 6880	1.33	2.01	1.5	1.72	0.2	0.11
Cont. 8015	1.18	1.69	1.43	1.48	0.15	0.1
Cont. 8900	1.14	1.52	1.33	1.38	0.11	0.08
Lyα	66.87	94.88	1.42	82.21	8.03	0.1
N v $\lambda\lambda$1238, 1242	18.87	32.7	1.73	24.23	3.54	0.15
Si iv $\lambda\lambda$1393, 1402	21.93	35.5	1.62	27.92	3.88	0.14
C iv $\lambda\lambda$1548, 1550	115.31	165.57	1.44	138.77	12.12	0.09
He ii λ1640	6.83	21.29	3.12	13.29	4.13	0.31
Hα	130.83	149.85	1.15	141.35	4.83	0.03
Hβ	38.29	45.4	1.19	42.32	1.94	0.05
Hγ	18.82	24.38	1.3	21.91	1.29	0.06
Hδ	7.17	10.92	1.52	9.13	0.94	0.1
He ii λ4685	11.93	17.7	1.48	14.82	1.6	0.11
He i λ5875	8.53	13.82	1.62	11.58	1.01	0.09
O i λ8446	7.47	9.13	1.22	8.32	0.37	0.04

4.3.1 Variability Statistics

To quantify the variability of the emission lines and continua variability statistics the definition by Rodriguez-Pascual et al. 1997 are adopted. They name the maximum-to-minimum flux ratio R_{max} and the fractional variability F_{var} as two common measures of variability. R_{max} is defined as the ratio of the the extreme of the integrated fluxes, F_{min} and F_{max}, and F_{var} as:

$$F_{\mathrm{var}} = \frac{\sqrt{\sigma_F^2 - \Delta^2}}{\langle F \rangle} \tag{4.1}$$

Here, σ_F^2 denotes the standard deviation, $\langle F \rangle$ the mean flux and Δ^2 the mean square value of the flux uncertainties, which is defined by:

$$\Delta^2 = \frac{1}{N} \sum_{i=1}^{N} \Delta_i^2 \tag{4.2}$$

The results for all parameters can be found in the Tables 4.3.

The obtained R_{max} and F_{var} values of the continuum lightcurves, show a decreasing trend towards continua around higher wavelengths. While the UV continuum around 1150 Åexhibits the highest values for $R_{\mathrm{max}} = 2.58$ and $F_{\mathrm{var}} = 0.28$, they continuously drop towards the most red continua which shows values of $R_{\mathrm{max}} = 1.33$ and $F_{\mathrm{var}} \simeq 0.08$.

The lightcurves of the Balmer emission lines exhibit lower variability, which increases towards the higher-order Balmer lines, with values between $R_{\mathrm{max}} \simeq 1.15 - 1.52$ and $F_{\mathrm{var}} \simeq 0.03 - 0.1$. The helium lightcurves show a similar variability to Hδ with values between $R_{\mathrm{max}} \simeq 1.48 - 1.62$ and $F_{\mathrm{var}} \simeq 0.09 - 0.11$ and the OI $\lambda 8446$ a similar variability to the Balmer lines with $R_{\mathrm{max}} \simeq 1.22$ and $F_{\mathrm{var}} \simeq 0.04$.

The variability of the emission line lightcurves in the UV region is on a similar level as that of the helium light curves in the optical region, with $R_{\mathrm{max}} \simeq 1.42 - 1.62$ and $F_{\mathrm{var}} \simeq 0.14$, with the exception of the He II $\lambda 1640$ lightcurve, which shows significant higher variability with $R_{\mathrm{max}} \simeq 3.12$ and $F_{\mathrm{var}} \simeq 0.31$.

4.3.2 Uncertainties Estimation

The uncertainties of the continuum and emission-line light curves are estimated based on the spectral noise and a systematic uncertainty introduced by the inter-calibration.

For the continuum light curves, the per-epoch noise is estimated as

$$\sigma_i^{\text{cont}} = \frac{\sigma_{f_i}}{\sqrt{N}}, \tag{4.3}$$

where σ_{f_i} denotes the standard deviation of the flux density within the selected continuum window in epoch i, and N is the number of pixels within that window. For the emission-line light curves, the noise is estimated from the scatter in the interpolated pseudo-continuum, σ_i^{noise} , as

$$\sigma_i^{\text{line}} = \frac{\sigma_i^{\text{p.cont.}} \Delta\lambda}{\sqrt{N}}, \tag{4.4}$$

where $\Delta\lambda$ denotes the integration range of the emission line and N is the number of pixels across the integration window.

As each epoch has been scaled to the flux of the narrow [O III] $\lambda5007$ line after the intercalibration, the systematic uncertainty introduced by the intercalibration is estimated from its fractional variability, $F_{\text{var}}^{[\text{O III}]\,\lambda5007}$:

$$\sigma_i^{\text{cal.}} = F_{\text{var}}^{[\text{O III}]\,\lambda5007} f_i. \tag{4.5}$$

The total uncertainty of the measured flux at epoch i, f_i, is then given with

$$\sigma_i^{\text{tot}} = \sqrt{(\sigma_i^{\text{cal.}})^2 + (\sigma_i^{\text{cont}})^2}, \tag{4.6}$$

for the continuum light curves and

$$\sigma_i^{\text{tot}} = \sqrt{(\sigma_i^{\text{cal.}})^2 + (\sigma_i^{\text{line}})^2}, \tag{4.7}$$

for the emission line light curves.

4.4   Time Lag

The time lag of the measured emission lines relative to the ionizing continuum is determined from the lag between the emission-line light curve and the UVW2 light curve. The time lag between two lightcurves is measured, by determining the cross-correlation function (CCF) of these curves and measuring the centroid of the CCF for values above 80% of the peak, as described in Section 2.2.2. This calculation is done with GECHO, which applies the interpolated cross-correlation function (ICCF) method introduced by Gaskell & Peterson 1987. The emission-line and ref-

erence light curves are normalized by subtracting the respective mean value from each data point. To increase the effective sampling and to measure the correlation between two unevenly sampled light curves, flux values between data points are linearly interpolated for both light curves.

The normalized light curves and the resulting CCFs are presented in Figures 4.7 and 4.8. Additionally, the top panel of each figure displays the UVW2 light curve together with its auto-correlation function, while the bottom panel compares both lightcurves of the UVW2 and the UV continuum around 1150 Å and shows the corresponding CCF and time lag which has to be added for the final estimation of the characteristic BLR radii for each emission line. The resulting time lags towards the UVW2 continuum and the corresponding characteristic BLR radii are listed in Table 4.4. The centroid uncertainties are estimated using the flux randomization/random subset selection (FR/RSS) method described by Peterson et al. 1998, with 10000 iterations and a lag bin size of 0.5 days (see Section 2.2.2). The resulting centroid distribution is displayed by the gray histogram in the above named figures.

Overall, the CCFs of all measured emission lines show strong correlations with pronounced peak values between ~ 0.7 and ~ 0.9, except for the CCF of O I 8446, which exhibits two local maxima at values of around ~ 0.6.

Hα and Hβ lag behind the UVW2 light curve by $3.3^{+1.1}_{-0.6}$ and $2.3^{+1.0}_{-0.3}$ days, respectively, while Hγ and Hδ show shorter lags of $1.7^{+0.2}_{-0.4}$ and $1.7^{+0.4}_{-0.4}$ days. Therefore the lower order Balmer lines Hα and Hβ show higher time lags, that the higher ordered Balmer lines Hγ and Hδ. Lyα exhibits a even shorter time lag than the Balmer lines with $1.0^{+0.4}_{-0.2}$ days within uncertainties, which implies that the hydrogen emitting region is stratified.

He I 5875 shows a lag of $3.3^{+0.7}_{-0.4}$ days, which is of the same order as the lags measured for Hα and Hβ within the uncertainties. Opposing to that, the two higher ionized He II 1640 and He II 4685 helium lines, shows much shorter lags, with a with $0.3^{+0.6}_{-0.2}$ days and $0.7^{+0.1}_{-0.3}$ days, respectively. The high ionized UV emission lines N v 1238, Si IV 1393 and C IV 1548 also show short time lags of about ~ 1 compared to the lower ionized Balmer and He I lines. Therefore a tendency becomes apparent, that the higher ionized emission lines typical show shorter time lags than the lower ionized emission lines.

While the low-ionized O I 8446 line exhibits and lag of $4.7^{+2.4}_{-1.4}$, which is slightly longer then the lag of Hα it should not be compared directly to UVW2, which is further discussed in section 4.7.
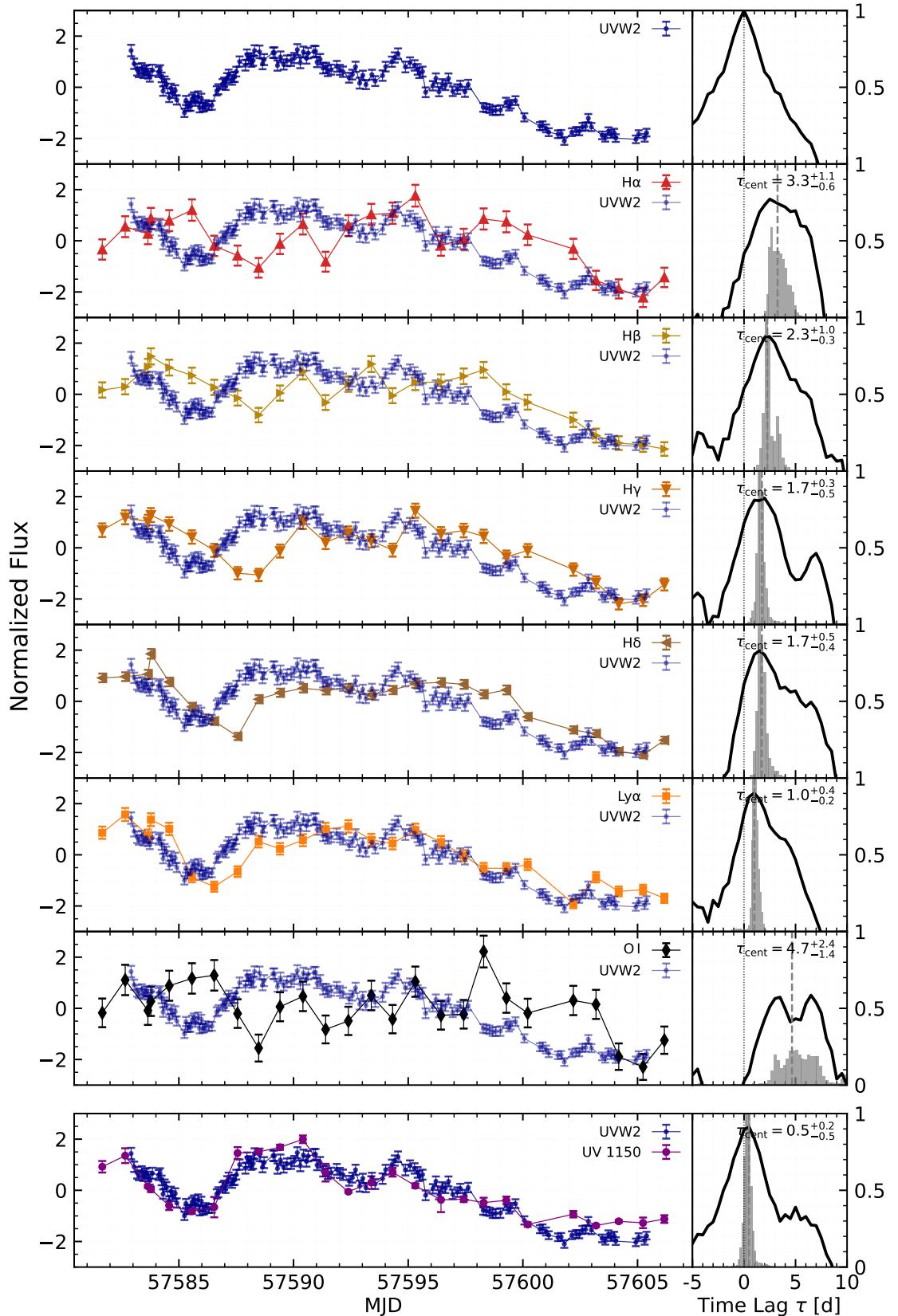
Figure 4.7: Comparison of normalized lightcurves and CCFs of Hα, Hβ, Hγ, He I λ5875, He II λ4685 and O I λ8446 with UVW2 as reference lightcurve.
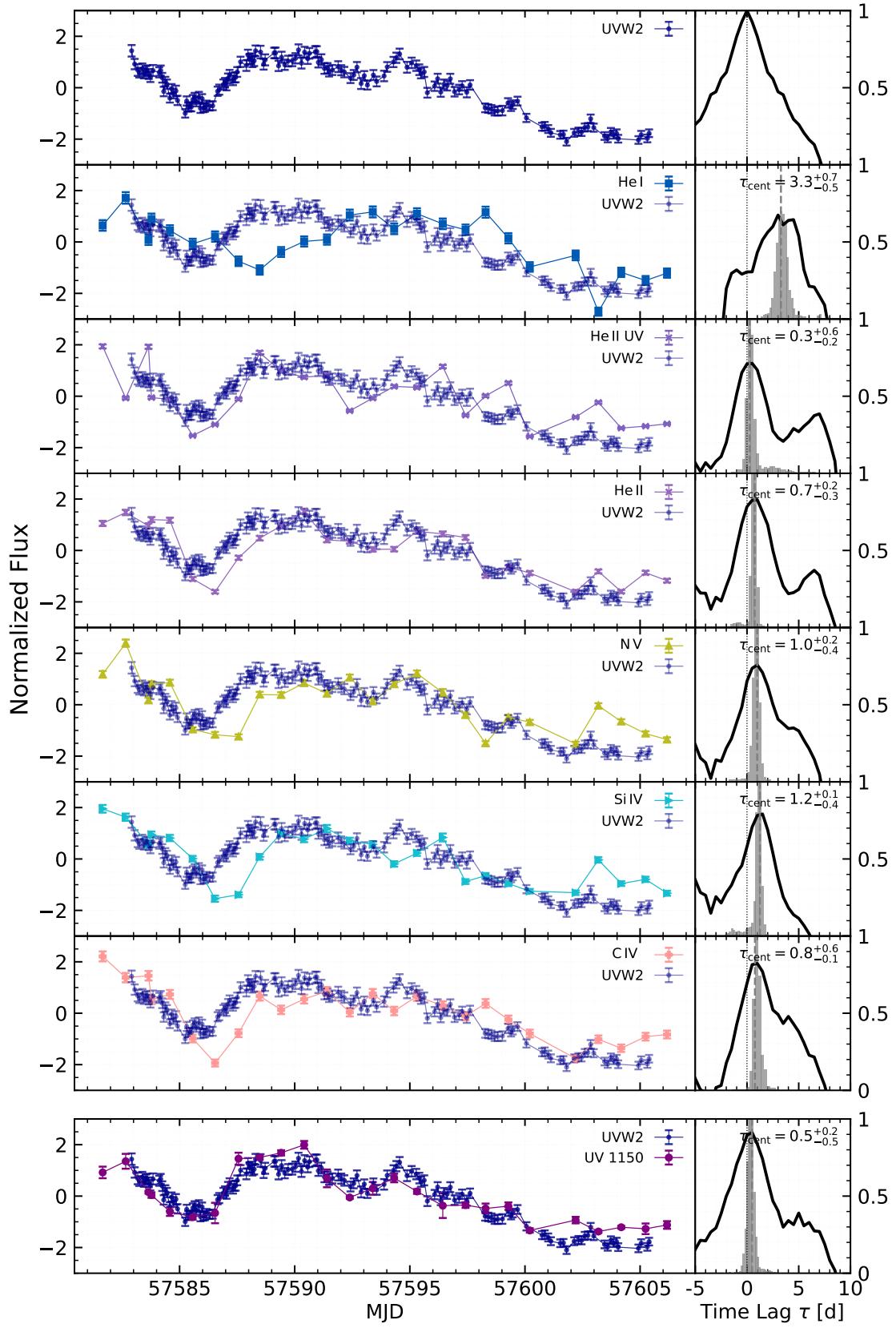
Figure 4.8: Comparison of normalized lightcurves and CCFs of UV lines with UVW2 as reference lightcurve.

Table 4.4: Centroid between the emission lines and UVW2 light curve and the characteristic BLR radii with an included shift of 0.5 light days due to the delay between UVW2 and the UV continuum around 1150 Å.

Line	τ_{cent} [d]	R_{BLR} [ld]
Hα	$3.3^{+1.1}_{-0.6}$	$3.8^{+1.1}_{-0.6}$
Hβ	$2.3^{+1.0}_{-0.3}$	$2.8^{+1.0}_{-0.3}$
Hγ	$1.7^{+0.2}_{-0.4}$	$2.2^{+0.2}_{-0.4}$
Hδ	$1.7^{+0.4}_{-0.4}$	$2.2^{+0.4}_{-0.4}$
Lyα	$1.0^{+0.4}_{-0.2}$	$1.5^{+0.4}_{-0.2}$
He I 5875	$3.3^{+0.7}_{-0.4}$	$3.8^{+0.7}_{-0.4}$
He II 1640	$0.3^{+0.6}_{-0.2}$	$0.8^{+0.6}_{-0.2}$
He II 4685	$0.7^{+0.1}_{-0.3}$	$1.2^{+0.1}_{-0.3}$
N V $\lambda\lambda$1238, 1242	$1.0^{+0.2}_{-0.4}$	$1.5^{+0.2}_{-0.4}$
Si IV $\lambda\lambda$1393, 1402	$1.2^{+0.1}_{-0.4}$	$1.7^{+0.1}_{-0.4}$
C IV $\lambda\lambda$1548, 1550	$0.8^{+0.5}_{-0.1}$	$1.3^{+0.5}_{-0.1}$
O I 8446	$4.7^{+2.4}_{-1.4}$	$5.2^{+2.4}_{-1.4}$

4.5 Line Profiles

The velocity dispersion of the BLR can be parameterized by the line widths of the broad emission line (Peterson et al. 2004) and is common in reverberation mapping campaigns(e.g. Kollatschny & Dietrich 1997; Denney et al. 2006). Therefore the line profiles of the emission lines are extracted from the mean and rms spectrum. Equally to the lightcurve extraction, a correction of the underlying continuum is necessary to enable comparison between the extracted profiles. Following the same procedure done for the lightcurves, an underlying linear continuum is interpolated, using line-free wavelength widows on the blue and red side for each emission line in both the mean and rms spectra. The selected boundaries of the pseudo-continua are listed in Table 4.5. By subtracting this interpolated continuum, a new zero-flux baseline for each line profile is defined. The flux is normalized to the maximum of each line profile and subsequently, the line profile is converted to velocity space using the relativistic Doppler equation (Sher 1968)

$$v_i = c \cdot \frac{\lambda_i^2 - \lambda_{\mathrm{central}}^2}{\lambda_i^2 + \lambda_{\mathrm{central}}^2}. \tag{4.8}$$

Here, λ_i denotes the wavelength values, $\lambda_{\mathrm{central}}$ the central wavelength of the emission line in rest-frame and c the speed of light. For the doublets N V $\lambda\lambda$1283, 1242, Si IV $\lambda\lambda$1393, 1402 and C IV $\lambda\lambda$1548, 1550 the rest-frame wavelength of the second line gets used as the central wavelength of the emission line. An overview of the

comparison of the mean and rms profiles for each emission line is displayed in Figure 4.9.

Comparing the mean and rms line profiles, the maxima of the rms profiles of the Balmer lines, Lyα and He I λ5875 show a shift towards positive velocities compared to the mean profile. Therefore most parts of the rms profiles is located within the red wing of the mean profiles. This implies that most of the variability of these lines emerge from the receding region of their emitting region. Opposing to that, the maxima of the rms profiles of the higher ionized helium lines He II λ1640 and He II λ4685 as well as from the high ionized UV emission lines N V $\lambda\lambda$1283, 1242, Si IV $\lambda\lambda$1393, 1402 and C IV $\lambda\lambda$1548, 1550 are found at the same location as for the mean profiles. With the exception for N V $\lambda\lambda$1283, 1242 which is blended with the Lyα profile, a more blue weighted rms profile can be seen for these emission lines.

The mean line profiles includes narrow components in addition to (Peterson 1997). A decomposition from the broad component was not attempted, since it was not possible to isolate the narrow component. Therefore the rms line profiles are used in the subsequent analysis to examine the kinematics of the BLR, since their only include the variable broad component of the emission lines.

Table 4.5: Boundaries of the blue and red pseudo-continua used for the interpolation of underlying continua for line profile extraction.

| Line	Pseudo-Continua (avg) [Å]	Pseudo-Continua (rms) [Å]
Hα	$6194 - 6216, 6861 - 6900$	$6279 - 6301, 6742 - 6781$
Hβ	$4762 - 4774, 5085 - 5112$	$4762 - 4774, 4967 - 4984$
Hγ	$4197 - 4220, 4435 - 4450$	$4197 - 4220, 4417 - 4429$
Hδ	$4026 - 4033, 4197 - 4221$	$4006 - 4016, 4197 - 4211$
O I λ8446	$7999 - 8025, 8775 - 8798$	$8222 - 8238, 8748 - 8767$
He I λ5875	$5679 - 5697, 6044 - 6057$	$5736 - 5753, 6027 - 6045$
He II λ1640	$1461 - 1468, 1679 - 1685$	$1461 - 1468, 1679 - 1685$
He II λ4685	$4198 - 4225, 4762 - 4774$	$4543 - 4554, 4766 - 4778$
Lyα	$1151 - 1161, 1270 - 1285$	$1151 - 1161, 1340 - 1355$
N V $\lambda\lambda$1283, 1242	$1151 - 1161, 1270 - 1285$	$1151 - 1161, 1340 - 1355$
Si IV $\lambda\lambda$1393, 1402	$1350 - 1360, 1430 - 1440$	$1340 - 1355, 1430 - 1440$
C IV $\lambda\lambda$1548, 1550	$1461 - 1468, 1679 - 1685$	$1461 - 1468, 1679 - 1685$
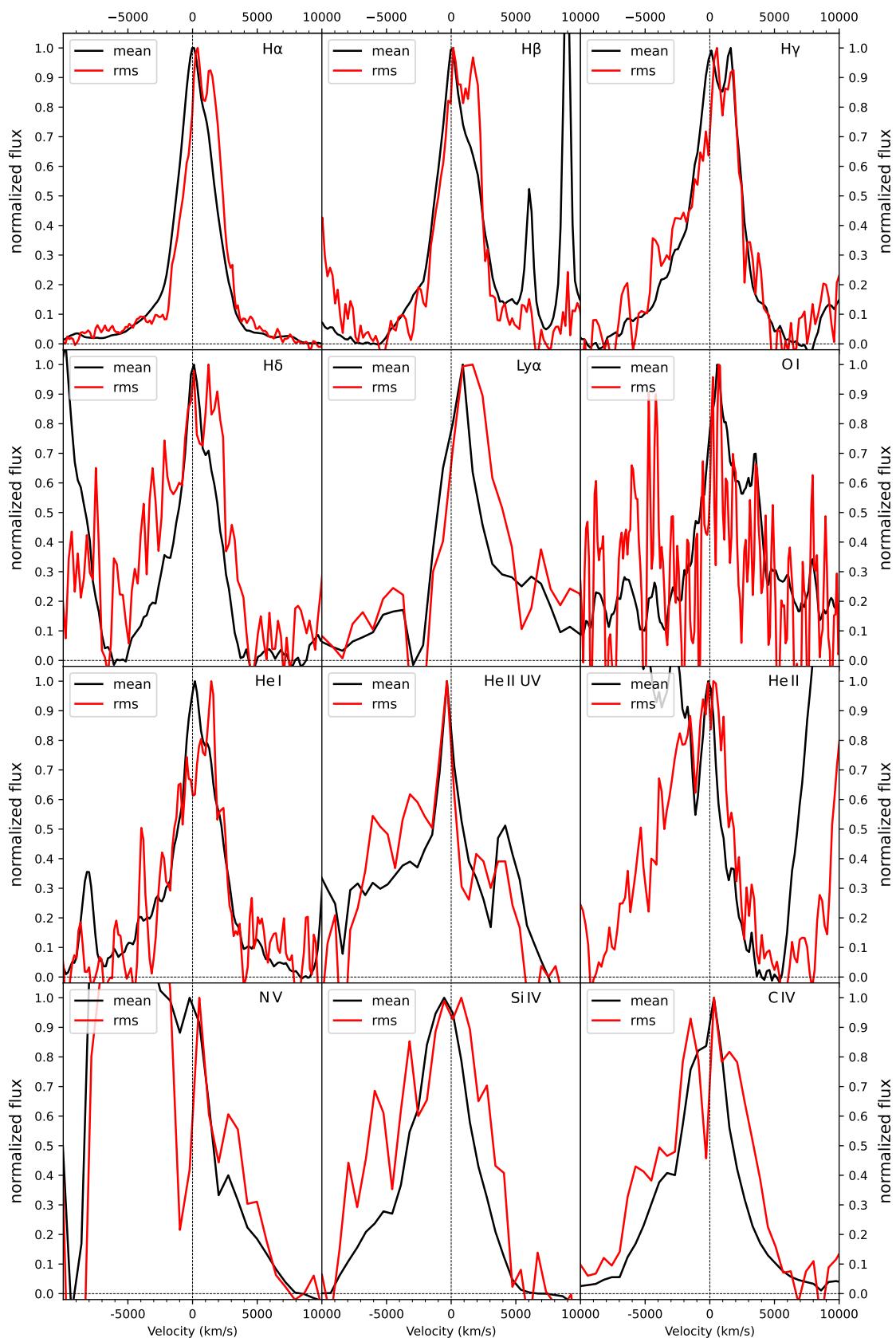
Figure 4.9: Normalized line profiles in the AVG and RMS spectra

4.5.1 FWHM estimation

Equally to earlier RM studies (e.g. Kollatschny & Dietrich 1997; Denney et al. 2006; Probst et al. 2025), the line width of the line profiles is estimated by their Full Width Half Maximum (FWHM), which is conducted with gecho. For this the height of the profiles is defined between the profiles maxima and the zero-flux base line. The mean profile of He II $\lambda4685$ is blended with Fe II emission in the blue wing, which makes a measurement of its FWHM not possible. Instead, the FWHM is estimated based on the width of its red wing, which is consistent with the order of magnitude of the FWHM of He II $\lambda1640$ within uncertainties.

The FWHM of profiles of O I $\lambda8446$, N V $\lambda\lambda1283$, 1242, and Si IV $\lambda\lambda1393$, 1402 were not measured due to following reasons.

The mean profile of the NIR emisson line O I $\lambda8446$ is blended with the Ca II $\lambda8498$, $\lambda8542$, $\lambda8662$ triplet. In a earlier study, Ochmann et al. 2025 was already able to decompose the line profile O I $\lambda8446$ based on a MUSE campaign in 2019, which is why this was not attempted in this analysis. While O I $\lambda8446$ exhibits variation in the rms spectrum, its profile is to noisy for a FWHM measurement due to the low signal to noise ratio.

The profiles of N V $\lambda\lambda1283$, 1242 is partly blended with the Lyα profile in both mean and rms and in addition exhibits absorption in its blue wing in the rms spectrum. Therefore it is not possible to measure reliable FWHM for the N V $\lambda\lambda1283$, 1242 profiles.

Finally, the profiles of Si IV $\lambda\lambda1393$, 1402 are blended with the semi-forbidden line doublet OIV] $\lambda\lambda1397$, 1400 and the FWHM of the profiles would therefore include this components in addition to the Si IV $\lambda\lambda1393$, 1402 component.

The resulting FWHM values are listed in Table 4.6. The uncertainties are estimated based on the instrumental dispersion of the gratings (see Table 3.1). The uncertainties are estimated primarily on the instrumental dispersion of the gratings (see Table 3.1) and selected higher accordingly the noise and shape of the profiles.

4.5.2 Comparison of the rms line profiles

The rms profiles of the Balmer line Hα – Hδ show a asymmetric double peaked shape with higher flux in the blue peak (see. 4.10). They show strong similarities, with the double-peaks located around $\sim 500\,\mathrm{km\,s^{-1}}$ and $\sim 2000\,\mathrm{km\,s^{-1}}$ for every profile. While the profiles of Hα and Hβ exhibiting similar steep slope in both wings as well, the Hγ and Hδ profiles show more extended blue wings. Therefore

Table 4.6: Measured FWHM and of the AVG and RMS line profiles.

Line	FWHM (avg)[km/s]	FWHM (rms)[km/s]
Hα	3000 ± 300	3100 ± 300
Hβ	3400 ± 300	3400 ± 300
Hγ	4100 ± 300	3900 ± 400
Hδ	3400 ± 300	5900 ± 1000
Lyα	3800 ± 350	4600 ± 500
He I $\lambda 5876$	3500 ± 300	4000 ± 400
He II $\lambda 1640$	2900 ± 500	6900 ± 1000
He II $\lambda 4686$	1800 ± 1000	6000 ± 400
C IV $\lambda\lambda 1548,\ 1550$	5400 ± 500	8400 ± 1000

the FWHM shows a increasing tendency towards the higher ordered Balmer lines with $3100 \pm 300\,\mathrm{km\,s^{-1}}$ and $3400 \pm 300\,\mathrm{km\,s^{-1}}$ for Hα and Hβ and $3900 \pm 400\,\mathrm{km\,s^{-1}}$ and $5900 \pm 1000\,\mathrm{km\,s^{-1}}$, respectively.

Comparing the rms profiles of the helium lines, differences in shape become apparent depending on the line ionization (see. Figure 4.11).

Compare helium lines

4.6 Black Hole Mass

The mass of the SMBH can be estimated by deriving the virial mass for each measured emission line and adjusting it with a scale factor f (Peterson et al. 2004). A scale factor of $f = 1.8$ is assumed, since FWHM of the RMS profiles is used to parameterize the velocity dispersion ΔV, following Probst et al. 2025 (see Section 2.2.3). O I $\lambda 8446$, N V $\lambda\lambda 1238,\ 1242$ and Si IV $\lambda\lambda 1238,\ 1242$ are excluded in the mass estimation, since they could not be measured reliably.

Taking equation 2.7, 2.8 and 2.9 the SMBH mass can be estimated based on the time lag and FWHM of for each emission line using:

$$M_{\mathrm{BH}} = 1.8 \cdot \frac{c \cdot \tau_{\mathrm{centroid}}\,\mathrm{FWHM}^2}{G}\,. \tag{4.9}$$

The resulting SMBH mass results, as well as the corresponding time lag and FWHM values of the broad emission lines are listed in Table 4.7.

To obtain a final estimation for the SMBH mass, a inverse-variance weighted mean is calculated. Since the uncertainties are asymmetric the higher gets adopted,
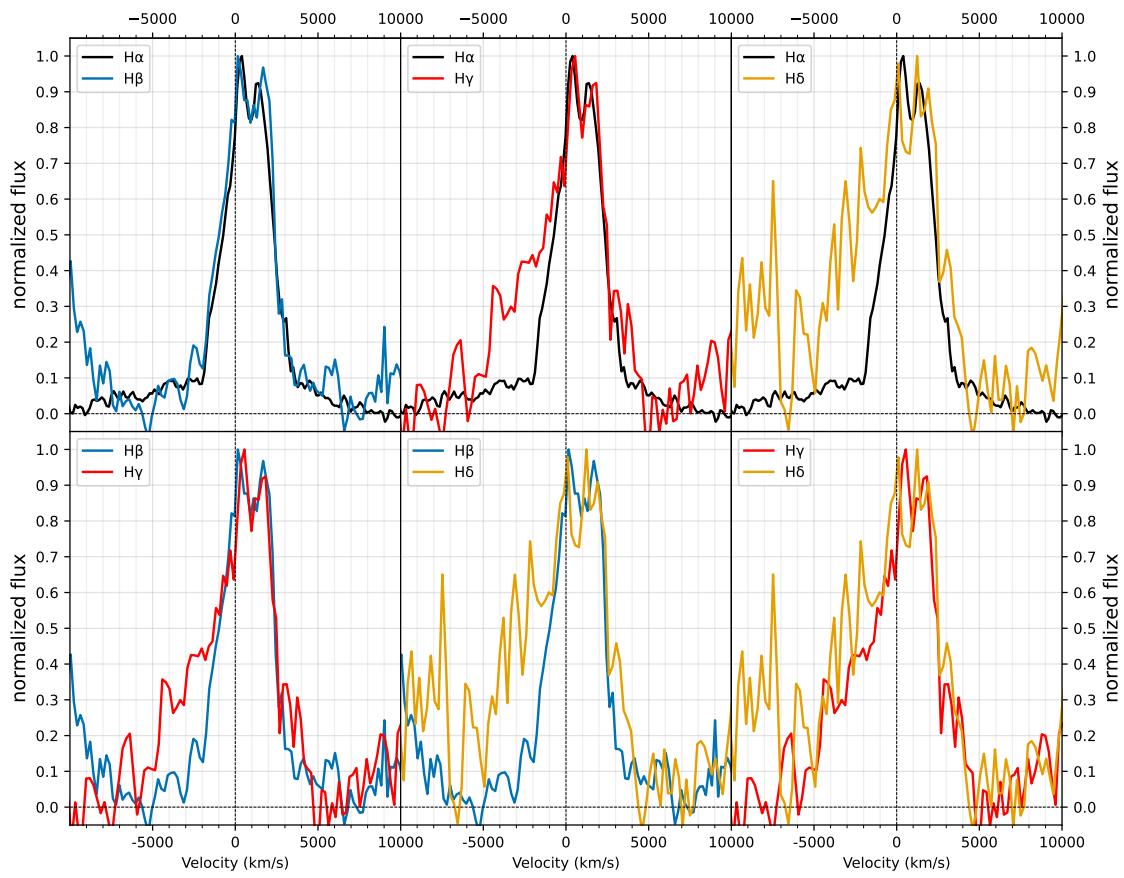
Figure 4.10: Comparison of the normalized RMS line profiles of the Balmer lines Hα, Hβ, Hγ and Hδ.
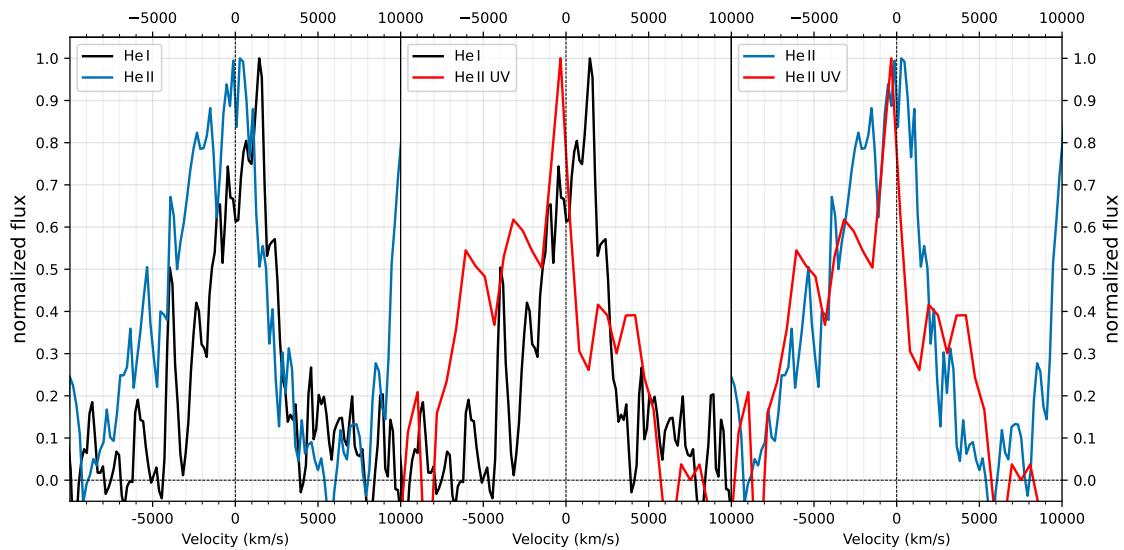
Figure 4.11: Comparison of the normalized RMS line profiles of the Helium lines

Table 4.7: Estimated characteristic BLR radii, FWHM and SMBH masses.

Line	R_{BLR} [ld]	FWHM (rms)[km/s]	$M_{\mathrm{BH}}[10^7 M_\odot]$
Lyα	$1.5^{+0.4}_{-0.2}$	4600 ± 500	$1.2^{+0.3}_{-0.2}$
Hα	$3.8^{+1.1}_{-0.6}$	3100 ± 250	$1.3^{+0.4}_{-0.2}$
Hβ	$2.8^{+1.0}_{-0.3}$	3400 ± 200	$1.2^{+0.5}_{-0.2}$
Hγ	$2.2^{+0.2}_{-0.4}$	3900 ± 300	$1.2^{+0.2}_{-0.3}$
Hδ	$2.2^{+0.4}_{-0.4}$	5900 ± 1000	$1.9^{+0.4}_{-0.4}$
He I $\lambda5876$	$3.8^{+0.7}_{-0.4}$	4000 ± 300	$2.1^{+0.4}_{-0.3}$
He II $\lambda1640$	$0.8^{+0.6}_{-0.2}$	6900 ± 1000	$1.3^{+1.0}_{-0.3}$
He II $\lambda4686$	$1.2^{+0.1}_{-0.3}$	6000 ± 300	$1.6^{+0.2}_{-0.4}$
C IV $\lambda\lambda1548,\ 1550$	$1.3^{+0.5}_{-0.1}$	8400 ± 1000	$3.2^{+1.3}_{-0.1}$

$\sigma_i = \max(\sigma_i^-, \sigma_i^+)$. The weighted mean is then given by

$$\bar{M}_{\mathrm{BH}} = \frac{\sum_i w_i M_{\mathrm{BH},i}}{\sum_i w_i}, \qquad w_i = \frac{1}{\sigma_i^2}, \tag{4.10}$$

with an uncertainty

$$\sigma_{\bar{M}} = \left(\sum_i w_i\right)^{-1/2}. \tag{4.11}$$

This gives a weighted-mean SMBH mass of $\bar{M}_{\mathrm{BH}} \approx (1.40 \pm 0.12) \times 10^7\, M_\odot$.

It has to be noted, that the scale factor of $f = 1.8$ does not account the low-inclination $i \sim 11°$ of the elliptic accretion disk, modeled in Ochmann et al. 2025. Adopting the scaling relation $f \sim \sin^{-2}(i)$ introduced by Krolik 2001, a value of $f \sim 27.5$ would be needed to account for the low inclination. Krolik 2001 used the line dispersion to parameterize the velocity dispersion, which is why the relation $\sigma_{\mathrm{line}} \approx \mathrm{FWHM}/2$ (Peterson et al. 2004) has to be accounted again. Due to the square relation of the velocity dispersion to the black hole mass seen in Equation 4.9, the scale factor finally gets corrected to a value $f \sim 6.8$. Subsequently the found BH mass has to be multiplied by a additional factor of 3.77. Subsequently, the weighted-mean SMBH mass can be estimated to be $\bar{M}_{\mathrm{BH}} \approx (5.28 \pm 0.12) \times 10^7\, M_\odot$.

4.7 Bowen Fluorescence of O I $\lambda8446$

Emission lines in the optical range, like the Balmer and helium lines, are commonly used in many reverberation-mapping campaigns, as they are easily accessible for nearby AGN (Peterson et al. 1991; Kollatschny & Dietrich 1997). This is not the case for the low-ionization line O I $\lambda8446$, which makes the emission line of particular interest in this analysis, since it exhibits noticeable variability (see. Table 4.3) and

therefore can be monitored in a RM analysis for the first time. O I $\lambda 8446$ is also know as a Bowen fluorescence line, that can be pumped by Lyβ emission (Grandi 1980). As described in Section 2.3, Lyβ excites O I through a near-resonant transition at $\lambda 1025$ Å. This is followed by decay via O I $\lambda 11287$ and subsequently by O I $\lambda 8446$, producing the observed O I $\lambda 8446$ emission (see Figure 2.5). This process was identified as the dominant excitation mechanism of O I $\lambda 8446$ in many other AGN (e.g. Rudy et al. 1989; Rodriguez-Ardila et al. 2002; Landt et al. 2008), showing that the variation in O I $\lambda 8446$ is caused by Lβ Bowen fluorescence. This also can be assumed for NGC 4593, since it is possible to rule-out recombination as a significant excitation mechanism of O I $\lambda 8446$ through analyzing line ratios. If recombination would drive the O I $\lambda 8446$ emission, a relative strength between O I $\lambda 8446$ and the quintet line O I $\lambda 7774$ of $\lambda 7774 / \lambda 8446 \approx 1.1 - 1.7$ should be detectable Grandi 1980; Landt et al. 2008. While O I $\lambda 7774$ is not detectable in the HST dataset, it is possible to determine a line ratio $\lambda 7774 / \lambda 8446 = 0.2$ based on the Muse spectrum of NGC 4593 presented by Ochmann et al. 2025, whic was taken in 2019. Therefore it can be assumed that the O I $\lambda 8446$ variation in NGC 4593 is driven through Bowen fluorescence, which enables to examine the Bowen fluorescence relation of O I $\lambda 8446$ for the first time in a RM analysis.

While Lyβ is not covered in the spectral range of the HST dataset, it is possible to use Lyα as a proxy for Lyβ, since it is expected that both lines arise under similar physical conditions. Therefore, the time lags between the UVW2 and emission-line lightcurves, as well as the CCFs and time lags between O I $\lambda 8446$ and Lyα, between Hα and Lyα, and between O I $\lambda 8446$ and Hα, are calculated and shown in Figure 4.12. All lightcurve show a strong correlation between $\sim 0.75 - 0.8$, with the exception of the O I $\lambda 8446$ and UVW2 lightcurves, which show a maximum correlation of only 0.6. The time lags and their uncertainties are calculated as before. O I $\lambda 8446$ lags behind Lyα by $2.5^{+1.7}_{-0.3}$ days and behind UVW2 by $4.7^{+2.4}_{-1.4}$ days, while Hα lags behind Lyα by $1.8^{+0.5}_{-0.5}$ days and behind UVW2 by $3.3^{+1.1}_{-0.6}$ days. Therefore the direct relation of O I $\lambda 8446$ to UVW2 shows a slightly higher lag than Hα to UVW2 within uncertainties. Assuming Bowen fluorescence as the dominant excitation mechanism the lag of O I $\lambda 8446$ should be estimated following the Bowen fluorescence path. With the Lyα light curve lagging behind the UVW2 light curve by $1.0^{+0.4}_{-0.2}$ days, this suggests a lag along the Bowen-fluorescence path from UVW2 to Lyα and from Lyα to O I $\lambda 8446$ sums to ~ 3.5 days. Therefore, O I $\lambda 8446$ shows a lag much closer and consistent with the lag of Hα within uncertainties. Looking at the O I $\lambda 8446$ and Hα lightcurves, they also show a strong correlation, with O I $\lambda 8446$ lagging behind Hα by about $0.3^{+1.6}_{-0.1}$ days, which is consistent with the lag found for the Bowen

fluorescence path.
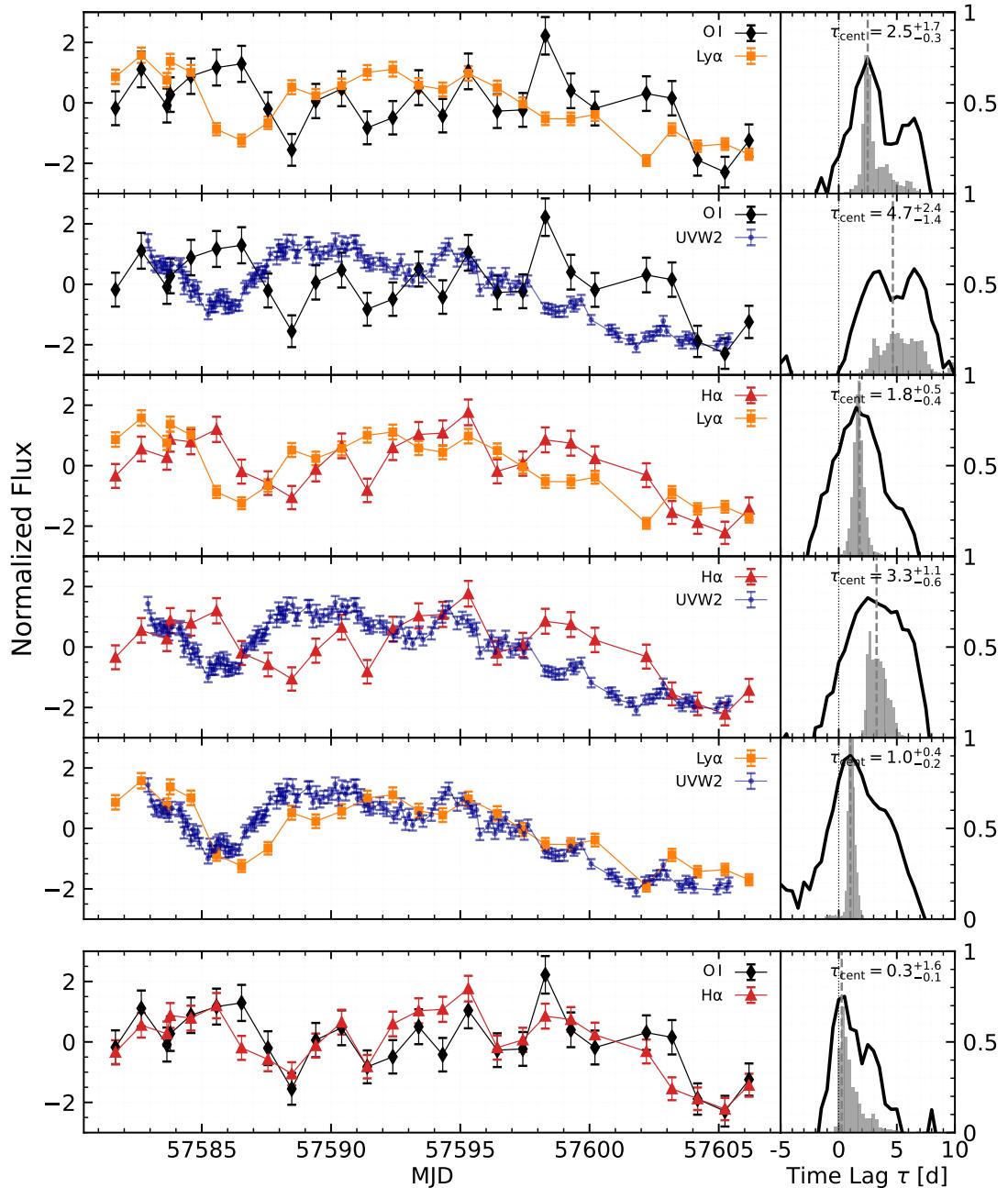
Figure 4.12: Comparison of normalized lightcurves and CCFs for Bowen Fluorescence.

5. Discussion

The nearby Seyfert I galaxy NGC 4593 has been monitored in several earlier RM studies (e.g. Kollatschny & Dietrich 1997; Denney et al. 2006; Cackett et al. 2018). In a recent study, Cackett et al. 2018 conducted an observing campaign of NGC 4593 with HST (PI: Cackett, E.M, Prop ID 14121), covering the optical to near-infrared range between $\sim 3900\,\text{Å}$–$9000\,\text{Å}$ as well as the UV range between $\sim 1100\,\text{Å}$–$1700\,\text{Å}$. Only a few other AGN have been monitored by HST, and the high cadence of nearly daily observations makes this campaign of particular interests for a RM campaign. This enabled a RM analysis of the BLR of NGC 4593 based on a HST/STIS campaign for the first time, including broad emission lines that had not previously been monitored (e.g. UV lines), and allowed an examination of the BLR structure of the galaxy. In addition the Bowen fluorescent emission line O I $\lambda 8446$ was included. Given the wavelength coverage of the campaign, it was possible to examine its Bowen fluorescence relation to Lyβ, which has not previously been monitored in a RM campaign. Also, the UV continuum around $1150\,\text{Å}$ was used as a proxy for the ionizing continuum instead of an optical continuum, as adopted in earlier works (e.g. Kollatschny & Dietrich 1997; Denney et al. 2006), since it is assumed to originate closer to the SMBH (Collin-Souffrin & Lasota 1988). The more densely sampled *Swift* UVOT UVW2 light curve presented by McHardy et al. 2018 has was compared to the light curve of the $1150\,\text{Å}$ continuum and showed a strong similarity. Owing to its higher cadence, the UVW2 light curve is adopted as the reference light curve for the RM analysis presented here. This analysis covered the UV emission lines Lyα, N V $\lambda\lambda 1238$, 1242, Si IV $\lambda\lambda 1393$, 1402, C IV $\lambda\lambda 1548$, 1550 and He II $\lambda 1640$, the optical emission lines Hα - Hδ, He II $\lambda 4686$ and He I $\lambda 5876$ and the NIR emission line O I $\lambda 8446$, which allowed a extended structural analysis of the BLR of NGC 4593 compared to earlier campaigns (Kollatschny & Dietrich 1997; Denney et al. 2006; Williams et al. 2018).

5.1 Structure of the BLR

5.1.1 Time Lags

The extracted light curves of the emission lines showed an overall similar shape, with strong correlation with the UVW2 light curve and CCF peak values between 0.7–0.9. Only the O I $\lambda 8446$ light curve showed a lower peak correlation with UVW2 of 0.6, as its variability is primary driven through Bowen fluorescence, which will be further discussed in Section 5.3.

Hα and Hβ showed different time lags of $3.3^{+1.1}_{-0.6}$ and $2.3^{+1.0}_{-0.3}$ days which are in good agreement with the results of earlier works (Kollatschny & Dietrich 1997; Denney et al. 2006; Williams et al. 2018). The higher-order Balmer lines Hγ and Hδ show a significantly shorter time lags with $1.7^{+0.2}_{-0.4}$ days and $1.7^{+0.4}_{-0.4}$ days, which follows the trend seen in other Seyfert galaxies that higher ordered Balmer lines show shorter time lags compared to the lower ordered Balmer lines (e.g. Gaskell & Sparke 1986; Kollatschny et al. 2001). It was also possible to infer the time lag of Lyα, which shows a even shorter time lag of $1.0^{+0.4}_{-0.2}$ days.

The helium lines show differences in time lag as well, depending on their ionization. He I $\lambda 5876$ lags $3.3^{+0.7}_{-0.4}$ days behind UVW2, while the higher-ionized He II $\lambda 1640$ and He II $\lambda 4686$ exhibit a much faster response times, with lags of $0.3^{+0.6}_{-0.2}$ days and $0.7^{+0.1}_{-0.3}$ days, respectively. Therefore the emitting region of He I is located at the same distance as the Hα weighted BLR, while the He II lines originate much shorter distance to the ionizing continuum. The high-ionized UV lines all show similar lags within uncertainties, with measured values of $1.0^{+0.2}_{-0.4}$, $1.2^{+0.1}_{-0.4}$ and $0.8^{+0.5}_{-0.1}$ days for N V $\lambda\lambda 1238$, 1242, Si IV $\lambda\lambda 1393$, 1402 and C IV $\lambda\lambda 1548$, 1550, respectively. Therefore, the broad emission lines show a tendency that higher ionized broad emission lines exhibit shorter time lags than lower ionized broad emission lines, which implies an ionization stratification structure of the BLR that has been reported in other Seyfert galaxies as well (e.g Collin-Souffrin & Lasota 1988; Gaskell & Sparke 1986; Kollatschny et al. 2001).

Since UVW2 lags behind the extracted HST/STIS 1150 Å continuum by approximately 0.5 days, this offset was added for the final estimation of the BLR radii for each emission line (see. 4.4).

5.1.2 Line Profiles

To draw conclusions about the kinematics of the BLR, the RMS line profiles of the broad emission lines have been obtained.

The Balmer line profiles show a similar asymmetric, double-peaked structure and are shifted toward positive velocities. This shift is also noticeable in the Lyα profile and He I λ5876 profile. This indicates that most of the line variability of these lines originates from the receding part of the emitting region.

Opposing to that, the maxima of the higher-ionization He II λ1640 and He II λ4686 profiles are located around their rest-frame wavelengths. A similar behavior is observed in the RMS profiles of the high-ionized UV lines N V $\lambda\lambda$1238, 1242, Si IV $\lambda\lambda$1393, 1402 and C IV $\lambda\lambda$1548, 1550. High-ionized broad emission lines often show a blue-shift compared to lower-ionized broad emission lines (Gaskell 1982), which could be an explanation for the shift in the RMS profile.

Hα and Hβ show comparatively steeper blue wings, whereas Hγ and Hδ exhibit more extended blue wings. The measured FWHM values of Hα with $3100 \pm 300\,\mathrm{km\,s^{-1}}$ agree well with previously reported line widths, while Hβ with $3400 \pm 300\,\mathrm{km\,s^{-1}}$ shows a slightly smaller value(e.g. Kollatschny & Dietrich 1997; Denney et al. 2006). The broader blue wings of Hγ and Hδ result in higher FWHM values of $3900 \pm 400\,\mathrm{km\,s^{-1}}$ and $5900 \pm 1000\,\mathrm{km\,s^{-1}}$, respectively. Ly$\alpha$ exhibits a slightly higher FHWM in its rms profile than the lower ordered Balmer lines as well, with $4600 \pm 500\,\mathrm{km\,s^{-1}}$.

The RMS profiles of the helium lines exhibit an extended blue wing and a steep red wing with the He II lines showing broader line widths. This results in FWHM values of $4000 \pm 400\,\mathrm{km\,s^{-1}}$ for He I λ5876, and broader values of $6000 \pm 400\,\mathrm{km\,s^{-1}}$ for He II λ4686 and $6900 \pm 1000\,\mathrm{km\,s^{-1}}$ for He II λ1640, respectively. The line profiles of the high-ionized UV lines partly exhibit absorption and high noise level, which results in significantly higher uncertainties than for the other emission lines. The FWHM of the Si IV $\lambda\lambda$1393, 1402 RMS profile could not be reliably estimated due to possible blending with O IV] emission, which cannot be separated from its profile. The FWHM of the rms profile of the N V $\lambda\lambda$1238, 1242 douplet could not reliably estimated as well, since it is partly blended with the red wing of Lyα and exhibits absorption in the blue wing. This leaves the C IV $\lambda\lambda$1548, 1550 rms profile with a FWHM of $8400 \pm 500\,\mathrm{km\,s^{-1}}$.

Comparing the FWHM values (see Table 4.6), a clear trend can be noted: higher-ionization broad emission lines tend to exhibit larger FWHM values than lower-ionization broad emission lines. This suggests that the emitting region of the higher-ionization lines exhibit higher velocities than the emitting region of the lower-ionization lines, which is consistent with the inferred ionization stratification of the BLR based on the time lag.

5.2 Black Hole Mass

Based on the reverberation mapping results, virial products were derived for the selected emission lines, and the SMBH mass was estimated using a scale factor of $f = 6.9$. The adopted scale factor accounts for the low inclination angle of $i \sim 11°$ reported by Ochmann et al. 2024. Its estimation is based on the relation $f \sim \sin^{-2}(i)$ (Krolik 2001), which captures the inclination dependence of the observed line-of-sight velocity dispersion. Since the velocity width is parameterized via the FWHM in this work rather than the line dispersion, an additional conversion was applied using $\sigma_{\text{line}} \approx \text{FWHM}/2$ (Peterson et al. 2004). Using this approach, an inverse-variance–weighted mean BH mass of $\bar{M}_{\text{BH}} \approx (5.28 \pm 0.12) \times 10^7 \, M_\odot$ was obtained from the determined values of each suitable emission line. Earlier works reported values in the same order of magnitude, e.g. $M \approx 1.4 \times 10^7 \, M_\odot$ (Kollatschny & Dietrich 1997) and $M = (9.8 \pm 2.1) \times 10^6 \, M_\odot$ (Denney et al. 2006). Using a similar approach, Kollatschny & Dietrich 1997 monitored Hα and estimated the SMBH mass using a scale factor of 1.5, whereas Denney et al. 2006 monitored Hβ and used a scale factor of 5.5. Rescaling these values to the scale factor of 6.9 used here yields $M \approx 6.44 \times 10^7 \, M_\odot$ (Kollatschny & Dietrich 1997) and $M = (1.23 \pm 0.26) \times 10^7 \, M_\odot$ (Denney et al. 2006). Therefore, the SMBH mass found in this analysis is consistent in order of magnitude with these earlier estimates.

5.3 Variation and Bowen Fluorescence of O I $\lambda 8446$

The low-ionization line O I $\lambda 8446$ was included in the RM analysis, as it exhibits noticeable variability in its RMS spectrum and is known to be a Bowen fluorescence line pumped by Lyβ emission (Grandi 1980). Although Lyβ is not covered in the HST dataset, Lyα was used as a proxy for investigation of the Bowen fluorescence O I $\lambda 8446$. As described in Section 2.3, Lyβ excites O I through a near-resonant transition at $\lambda 1025$ Å. This is followed by decay via O I $\lambda 11287$ and subsequently by O I $\lambda 8446$, producing the observed O I $\lambda 8446$ emission (see Figure 2.5). This cascade is expected to occur with a photon ratio of 1:1 (Grandi 1980). A photon ratio of ~ 0.8 between O I $\lambda 8446$ and O I $\lambda 11287$, which was taken from the near-infrared SpeX spectra obtained by Landt et al. 2008, was determined. This result shows that Lyβ pumping is the dominant excitation mechanism in O I $\lambda 8446$ in NGC 4593.
In addition, the comparison shown in Figure 4.12 demonstrates that O I $\lambda 8446$ exhibits a significantly stronger correlation with Lyα than with UVW2, further supporting this interpretation. Therefore, the emitting region of O I is likely located at

a distance corresponding to a lag of ~ 3.5 days from the ionizing continuum, consistent with the Bowen fluorescence scenario, rather than the $4.7^{+2.4}_{-1.4}$ days implied by the direct lag relative to UVW2 under the assumption of recombination as the main excitation mechanism. With that, the Bowen fluorescence lag of O I corresponds to the radius of the emitting region of Hα with $3.3^{+1.1}_{-0.6}$ days. Since Hα and O I $\lambda\,8446$ also exhibits a strong correlation with a minimal time shift of ~ 0.3 days, it can be inferred that O I $\lambda\,8446$ is emitted at approximately the same radius as Hα within uncertainties.

5.4   Summary

This thesis presents the results of the first reverberation-mapping analysis of the broad-line region (BLR) of the Seyfert I galaxy NGC 4593 based on an HST/STIS campaign (PI: Cackett, E.M, Prop ID 14121). This dataset is ideally suited for reverberation mapping thanks to its daily cadence and its broad wavelength coverage spanning parts of the UV and the optical-to-NIR regimes. This enabled a more detailed investigation of the BLR structure than in previous RM studies of NGC 4593 by including additional broad emission lines that had not been covered before. The measured time lags and FWHM values are listed in Tables 4.4 and 4.6, respectively. The results indicate a systematic trend: higher-ionization broad emission lines exhibit shorter time lags and broader line widths than lower-ionization lines, indicating an ionization stratified BLR (Collin-Souffrin & Lasota 1988).

Based on the virial products of the reverberation-mapped lines, a SMBH mass of $\bar{M}_{\mathrm{BH}} \approx (5.28 \pm 0.12) \times 10^7\ M_\odot$ was inferred, which agrees in order of magnitude with earlier estimates (e.g. Kollatschny & Dietrich 1997; Denney et al. 2006).

In addition, variability of the low-ionization line O I $\lambda\,8446$ was detected for the first time in a reverberation-mapping analysis. It was show that this variability is majorly driven through Lyβ fluorescence, making O I $\lambda\,8446$ the first Bowen-fluorescence line investigated with RM. Following the Bowen-fluorescence process, the emitting region was approximately found at the same distance as the emitting region of Hα towards the ionizing continuum. The results of the analysis of the O,I,λ, 8446 variability led to a publication (Ochmann et al. 2026).

Bibliography

Aladin Lite (2025). CDS (Centre de Données astronomiques de Strasbourg). URL: `https://aladin.cds.unistra.fr/AladinLite/` (visited on 07/19/2025).

Anderson, J. & L. R. Bedin 2010, *Publications of the Astronomical Society of the Pacific*, 122, 1035.

Antonucci, Robert 1993, *Annual Review of Astronomy and Astrophysics*, 31, 473–521.

Beckmann, Volker & Chris R. Shrader 2013, *The AGN phenomenon: open issues*, URL: `https://arxiv.org/abs/1302.1397`.

Bowen, I. S. 1934, *Publications of the Astronomical Society of the Pacific*, 46, 146–148.

Bowen, I. S. 1947, *Publications of the Astronomical Society of the Pacific*, 59, 196.

Cackett, E. M., C.-Y. Chiang, I. McHardy, et al. 2018, *The Astrophysical Journal*, 857, 53.

Collin-Souffrin, Suzy & Jean-Pierre Lasota 1988, *Publications of the Astronomical Society of the Pacific*, 100, 1041.

Czerny, Bozena & Krzysztof Hryniewicz 2011, *Astronomy and Astrophysics*, 525, L8.

Denney, K. D., M. C. Bentz, B. M. Peterson, et al. 2006, *Astrophysical Journal Letters*, 653, 152–158.

Dexter, J. & E. Agol 2010, *The Astrophysical Journal*, 727, L24.

Dietrich, M, W Kollatschny, D Alloin, et al. 1994, *Astronomy and Astrophysics*, 284, 33–43.

Gaskell, C Martin 1982, *Astrophysical Journal*, 263, 79–86.

Gaskell, C Martin 2009, *New Astronomy Reviews*, 53, 140–148.

Gaskell, C Martin & Linda S Sparke 1986, *The Astrophysical Journal*, 305, 175–186.

Gaskell, C. M. & B. M. Peterson 1987, *The Astrophysical Journal Supplement Series*, 65, 1.

Goad, M. R., K. T. Korista, & A. J. Ruff 2012, *Monthly Notices of the Royal Astronomical Society*, 426, 3086–3111.

Graham, A. W., C. A. Onken, E. Athanassoula, et al. 2011, *Monthly Notices of the Royal Astronomical Society*, 412, 2211–2228.

Grandi, S. A. 1980, *The Astrophysical Journal*, 238, 10.

Grier, C. J., P. Martini, L. C. Watson, et al. 2013, *The Astrophysical Journal*, 773, 90.

Horne, K., B. M. Peterson, S. J. Collier, et al. 2004, *Publications of the Astronomical Society of the Pacific*, 116, 465.

Hubble Advanced Spectral Products (HASP) (2025). Space Telescope Science Institute. URL: https://archive.stsci.edu/missions-and-data/hst/hasp (visited on 09/17/2024).

Keel, Bill (2002). *Quasars and Active Galactic Nuclei - Optical spectra of various kinds of active galactic nuclei*. Accessed: 2025-12-22. URL: https://pages.astronomy.ua.edu/keel/agn/spectra.html.

Kollatschny, W. & M. Dietrich 1997, *Astronomy and Astrophysics*, 323, 5–13.

Kollatschny, Wolfram, K Bischoff, EL Robinson, et al. 2001, *Astronomy and Astrophysics*, 379, 125–135.

Komossa, S. 2007, *Narrow-Line Seyfert 1 Galaxies*, URL: https://arxiv.org/abs/0710.3326.

Krolik, Julian H 2001, *The Astrophysical Journal*, 551, 72.

Landt, Hermine, Misty C Bentz, Martin J Ward, et al. 2008, *The Astrophysical Journal Supplement Series*, 174, 282.

McHardy, I. M., S. D. Connolly, B. M. Peterson, et al. 2017, *Monthly Notices of the Royal Astronomical Society*, 465, 273–289.

McHardy, IM, SD Connolly, K Horne, et al. 2018, *Monthly Notices of the Royal Astronomical Society*, 480, 2881–2897.

Mikulski Archive for Space Telescopes (MAST) (2025). Space Telescope Science Institute. URL: https://mast.stsci.edu/search/ui/#/hst (visited on 09/17/2024).

Mo, H., F. van den Bosch, & S. White 2010, *Galaxy Formation and Evolution*, Cambridge University Press.

NED (2025). *NASA/IPAC Extragalactic Database.* Operated by the Jet Propulsion Laboratory, California Institute of Technology, under contract with NASA. URL: https://ned.ipac.caltech.edu/ (visited on 07/19/2025).

Netzer, H. 2013, *The Physics and Evolution of Active Galactic Nuclei*, Cambridge University Press, Cambridge.

Netzer, H. & M. V. Penston 1976, *Monthly Notices of the Royal Astronomical Society*, 174, 319–325.

Ochmann, M. W., W. Kollatschny, M. A. Probst, et al. 2024, *Astronomy & Astrophysics*, 686, A17.

Ochmann, M. W., P. M. Weilbacher, M. A. Probst, et al. 2025, *Astronomy & Astrophysics*, 697, L5.

Ochmann, Martin W, Edward M Cackett, Lukas Diehl, et al. 2026, *Astronomy and Astrophysics*, 705, L11.

Onken, C. A., L. Ferrarese, D. Merritt, et al. 2004, *The Astrophysical Journal*, 615, 645–651.

Osterbrock, D. E. 1977, *The Astrophysical Journal*, 215, 733–745.

Osterbrock, D. E. 1981, *The Astrophysical Journal*, 249, 462–470.

Osterbrock, Donald E. & Richard W. Pogge 1985, *The Astrophysical Journal*, 297, 166–176.

Peterson, B. M. 1993, *Publications of the Astronomical Society of the Pacific*, 105, 247–268.

Peterson, B. M. 1997, *An Introduction to Active Galactic Nuclei*, Cambridge University Press.

Peterson, B. M., L. Ferrarese, K. M. Gilbert, et al. 2004, *The Astrophysical Journal*, 613, 682–699.

Peterson, B. M. & K. Horne 2004, *Astronomische Nachrichten*, 325, 248–251.

Peterson, B. M., I. Wanders, K. Horne, et al. 1998, *Publications of the Astronomical Society of the Pacific*, 110, 660.

Peterson, BM, TJ Balonek, ES Barker, et al. 1991, *Astrophysical Journal*, 368, 119–137.

Probst, M. A., W. Kollatschny, M. W. Ochmann, et al. 2025, *Emission-Line and Continuum Reverberation Mapping of the NLS1 Galaxy WPVS 48*, URL: https://arxiv.org/abs/2511.09153.

Rees, M. J. 1984, *Annual Review of Astronomy and Astrophysics*, 22, 471–506.

Ricci, C. & B. Trakhtenbrot 2023, *Nature Astronomy*, 7, 1282–1294.

Rodriguez-Ardila, Alberto, SM Viegas, Miriani Griselda Pastoriza, et al. 2002, *The Astrophysical Journal*, 572, 94–104.

Rodriguez-Pascual, PM, D Alloin, J Clavel, et al. 1997, *The Astrophysical Journal Supplement Series*, 110, 9.

Rudy, Richard J, George S Rossano, & RC Puetter 1989, *Astrophysical Journal*, 342, 235–237.

Seyfert, Carl K. 1943, *The Astrophysical Journal*, 97, 28–40.

Shakura, N. I. & R. A. Sunyaev 1973, *Astronomy and Astrophysics*, 24, 337–355.

Sher, D 1968, *Journal of the Royal Astronomical Society of Canada*, 62, 105.

STIS (2025). *STIS Instrument Handbook: Gratings*. URL: `https://hst-docs.stsci.edu/stisihb/chapter-13-spectroscopic-reference-material/13-3-gratings` (visited on 05/12/2025).

STScI (2025). *Digitized Sky Survey*. IPAC. DOI: `10.26131/IRSA441`. URL: `https://www.ipac.caltech.edu/doi/irsa/10.26131/IRSA441` (visited on 07/19/2025).

Ulrich, M.-H., L. Maraschi, & C. M. Urry 1997, *Annual Review of Astronomy and Astrophysics*, 35, 445–502.

Urry, C. M. & P. Padovani 1995, *Publications of the Astronomical Society of the Pacific*, 107, 803–845.

Véron-Cetty, M-P, P Véron, & AC Gonçalves 2001, *Astronomy and Astrophysics*, 372, 730–754.

Williams, Peter R., Anna Pancoast, Tommaso Treu, et al. 2018, *The Astrophysical Journal*, 866, 75.